Low-temperature indoor VOC oxidation over Pt catalysts: Interplay between zeolite acidity and framework architecture

Catalysis Today 478 (2026) 115978

Contents lists available at ScienceDirect

Catalysis Today

journal homepage: www.elsevier.com/locate/cattod

Low-temperature indoor VOC oxidation over Pt catalysts: Interplay between zeolite acidity and framework architecture

Alessia Cometto, Enrico Sartoretti *, Samir Bensaid *, Nunzio Russo

Department of Applied Science and Technology, Politecnico di Torino, Corso Duca degli Abruzzi, 24, Turin, 10129, Italy

ARTICLE INFO

Keywords:
Bifunctional catalysts
Platinum nanoparticles
Metal dispersion
ZSM-5 and SBA-15 supports
Support acidity
VOC oxidation
Low-temperature oxidation

ABSTRACT

In this study, platinum nanoparticles (0.5 wt%, <4 nm) were deposited on microporous ZSM-5 zeolites with different SiO_2/Al_2O_3 molar ratios and on mesoporous SBA-15 silica to investigate the influence of support properties on indoor VOC oxidation under mild conditions. TEM, CO chemisorption and XPS confirmed uniform particle size, high metal dispersion and predominantly metallic Pt on all catalysts, ensuring a direct comparison of support-dependent effects. Catalytic activity was evaluated for the oxidation of CO, ethylene and toluene at an indoor-relevant concentration of 100 ppm in air. CO oxidation started at room temperature and was mainly governed by exposed Pt sites, whereas support characteristics may contribute to the observed differences in low-temperature activity. For ethylene and toluene oxidation, Pt/ZSM-5 catalysts showed improved performance compared with Pt/SBA-15, suggesting that the physicochemical properties of the zeolitic support, including acidity and pore architecture, influence reactant adsorption and accessibility to catalytic sites. These findings provide useful guidelines for the design of efficient low-loading Pt-based catalysts for indoor air purification technologies.

1. Introduction

Volatile Organic Compounds (VOCs) constitute a broad and diverse class of atmospheric pollutants, defined by high vapour pressure, chemical heterogeneity and widespread presence in human environments [1]. They are emitted from numerous indoor and outdoor sources, including industrial activities, transportation, construction materials, consumer products and routine human behaviours [2]. Although VOCs are widespread in both outdoor and indoor environments, their impact on indoor air quality is particularly critical, as it is estimated that individuals in the United States spend around 90% of their time in enclosed spaces [3]. Such exposure has been associated with a range of adverse health outcomes. These range from short-term symptoms — such as eye irritation, headaches and respiratory discomfort — to long-term effects including allergies, asthma and, for specific compounds and exposure levels, carcinogenic risks [4]. A recent systematic review by Halios et al. (2022) [4], covering 92 European studies published between 2000 and 2022, identified more than 65 frequently occurring indoor VOCs, including aromatic hydrocarbons, alkanes, aldehydes, terpenes and chlorinated species. This chemical diversity highlights the complexity of indoor VOC mixtures and the challenges associated with monitoring and mitigation. Regulatory guidelines issued by international organisations — such as WHO, the European Union and the U.S. EPA — differ substantially in scope and stringency, reflecting the heterogeneous nature and sources of these pollutants [1,5,6].

Current control strategies for VOCs generally rely on either capture or destruction approaches. Adsorption-based methods — such as those employing activated carbon or other porous sorbents — can temporarily remove VOCs but they suffer from limitations, including rapid saturation and challenges related to regeneration or disposal [1,7]. Catalytic oxidation, by contrast, offers a more permanent solution by converting VOCs into carbon dioxide and water under relatively mild conditions [8,9]. Low-temperature operation is particularly advantageous for indoor applications, as it enables effective VOC oxidation under realistic operating conditions and reduces energy consumption. It can also minimize support and catalyst degradation, and improve safety in confined environments. Catalysts used for VOC oxidation typically fall into two categories: noble metal and transition-metal oxides. Noble metals, such as platinum (Pt) and palladium (Pd), exhibit high activity and CO_2 selectivity even at low temperatures; however, their high cost and susceptibility to deactivation by certain species, e.g., chlorinated compounds, limit their practical implementation [7,10].

* Corresponding authors.
E-mail addresses: enrico.sartoretti@polito.it (E. Sartoretti), samir.bensaid@polito.it (S. Bensaid).

https://doi.org/10.1016/j.cattod.2026.115978
Received 17 June 2026; Received in revised form 26 August 2026; Accepted 8 September 2026
Available online 13 September 2026

Transition-metal oxides, including Mn-, Co- and Cu-based materials, are more economical and generally more resistant to poisoning, but they typically require higher operating temperatures and present lower acidity [11,12]. Therefore, designing catalysts that deliver high performance while minimizing noble metal loading remains a key objective for indoor VOC abatement.

Extensive studies on Pt-based catalysts have demonstrated that the metal particle size and oxidation state play a crucial role in determining catalytic activity and selectivity. For example, Chen et al. [13] reported that Pt/ZSM-5 catalysts with a particle size around 1.9 nm exhibited optimal toluene oxidation performance, due to the balance between high dispersion and sufficient exposure of metallic Pt sites. Nevertheless, Pt nanoparticles are susceptible to aggregation even at moderate temperatures, which reduces the accessible active surface area and consequently decreases catalytic efficiency. Anchoring Pt on high-surface-area supports such as γ-Al_2O_3, ZSM-5, SBA-15 or MCM-41 can help mitigate nanoparticle sintering and enhance stability [10,14].

In the present work, ZSM-5 was selected as the support for nanoparticle deposition due to its high surface area (300–450 m^2/g), well-defined 10-membered ring channel system (5.3 × 5.6 Å and 5.1 × 5.5 Å), excellent thermal stability, shape selectivity and tailored acidity [10,15]. These characteristics make ZSM-5 one of the most extensively studied and industrially relevant zeolites, including for VOC oxidation applications [16]. In addition, zeolites are particularly attractive materials because their Brønsted acid sites can assist hydrocarbon activation by polarizing C-H and C=C bonds [10,17].

In contrast, SBA-15, a mesoporous silica, was employed as a low-acidity support due to its acidity being mainly limited to surface silanol groups and its elevated surface area (600–1000 $m^2\ g^{-1}$). SBA-15 exhibits a well-ordered hexagonal arrangement of cylindrical mesopores with diameters ranging from 5 to 30 nm, considerably larger than the targeted platinum nanoparticles [18,19]. According to Rosenholm et al. (2006) [20], SBA-15 displays dual surface acidity arising from two types of silanol groups: a minor fraction of strongly acidic Q^3 silanols (≈15–20%, pKa ≈ 2) and a predominant fraction of weakly acidic Q^2 silanols (≈80%, pKa ≈ 8–9).

Despite extensive research efforts, the combined influence of support acidity, pore architecture and Pt dispersion on VOC oxidation — particularly under mild, indoor-relevant conditions — remains insufficiently understood. To address this gap, we investigated low Pt-loading catalysts (0.5 wt%) supported on ZSM-5 with different SiO_2/Al_2O_3 molar ratios (50, 80 and 117) and on mesoporous SBA-15. Controlled impregnation and stirring-assisted deposition techniques were employed to obtain well-dispersed Pt nanoparticles. The catalytic activity was systematically investigated using carbon monoxide (CO) oxidation as a probe reaction for assessing the intrinsic oxidation ability of metallic Pt sites, while ethylene and toluene were selected as representative volatile organic compounds (VOCs). Ethylene is a small, unsaturated hydrocarbon belonging to the alkene family [11]. It also functions as a natural plant hormone, that regulates fruit ripening even at trace (ppm) concentrations. Its accumulation can therefore contribute to food spoilage during storage. Furthermore, ethylene is an important industrial feedstock for producing polyethylene, ethylene glycol and numerous chemical intermediates [17]. However, its accumulation in confined environments can accelerate degradation processes and contribute to photochemical smog formation [21,22]. Toluene, an aromatic VOC, was selected due to its widespread industrial relevance and environmental impact [23]. It is extensively used as a solvent in chemical manufacturing, printing, and fuel-related sectors. It is also emitted during various anthropogenic processes, including fuel and coke production [24]. Moreover, toluene is commonly found in consumer products such as paints, adhesives and rubber, contributing to its elevated levels in indoor air [25]. Due to its toxicity and persistence, the catalytic oxidation of toluene is considered a key pathway for VOC abatement in air purification systems [26].

Despite extensive research on Pt-based catalysts for VOC oxidation, the combined influence of support acidity and pore architecture under mild, indoor-relevant conditions remains insufficiently understood. To address this gap, Pt catalysts with a low metal loading (0.5 wt%) were prepared on ZSM-5 zeolites with different SiO_2/Al_2O_3 ratios and on mesoporous SBA-15. Particular attention was devoted to obtaining comparable Pt nanoparticle characteristics among the catalysts. This approach minimizes differences associated with the metallic phase and enables a more direct assessment of support effects. CO, ethylene and toluene oxidation were investigated at trace concentrations (100 ppm), closer to real indoor conditions but less commonly explored than the higher concentrations typically adopted in kinetic studies [11,17]. Catalytic testing was combined with detailed characterization of Pt dispersion and oxidation state, surface acidity, pore architecture and adsorption properties. This approach allowed to clarify how these support features govern VOC adsorption, accessibility to Pt sites, and oxidation performance. The resulting structure-property relationships provide a basis for the rational design of high-performance, low-Pt catalysts for VOC abatement.

2. Materials and methods

2.1. Catalyst synthesis

Three types of NH_4-ZSM-5 zeolites (Alfa Aesar), with SiO_2/Al_2O_3 molar ratios of 50, 80, and 117, were selected as catalyst supports. Prior to use, the materials were calcined at 550 °C in air for 4 h to convert them into the protonated form. This treatment increases the overall acidity of the zeolites and enhances their thermal stability during subsequent heat treatments [27]. SBA-15 (Sigma-Aldrich) was employed as the mesoporous reference support and was calcined at 350 °C in air for 4 h to remove residual pore-blocking species, thereby maximizing the accessible specific surface area [18].

Platinum nanoparticles were synthesized via the polyol reduction method, following established literature protocols [13,28,29]. The reagents used in the synthesis included chloroplatinic acid ($H_2PtCl_6{\cdot}6H_2O$, 8 wt%, Sigma-Aldrich), ethanol (Sigma-Aldrich), ethylene glycol (EG, Sigma-Aldrich), polyvinylpyrrolidone (PVP, Mw=40,000, Sigma-Aldrich), hydrochloric acid (HCl, 37%, Sigma-Aldrich) and sodium hydroxide (NaOH, Sigma-Aldrich).

Specifically, a NaOH solution in ethylene glycol (0.22 g in 20 mL) was slowly added to an EG solution of $H_2PtCl_6{\cdot}6H_2O$ (20 mL) under continuous stirring [30,31]. After 1 h of stirring at room temperature, a clear yellow suspension was obtained. The mixture was subsequently heated to 90 °C for 2 h under a nitrogen atmosphere, resulting in the formation of a stable dark colloidal solution containing Pt nanoparticles. After cooling to room temperature, an HCl solution (0.3 M) was added in a stoichiometric amount relative to the NaOH used. This ensured the quantitative formation of NaCl and minimized residual species that might inhibit the catalytic performance [32]. Finally, 40 mg of PVP was introduced into the suspension, which was vortex-mixed for one minute to ensure complete polymer dispersion.

Two deposition methods were employed to achieve 0.5 wt% of platinum loading on the supports, i.e. stirring and solvent-evaporation impregnation. A relatively low platinum loading was selected to remain within the range typically used in industrial applications [33]. In both procedures, a 25% excess of the Pt nanoparticle suspension was used to compensate for possible platinum losses during washing and separation, ensuring that the final metal loading approached the target value of 0.5 wt%.

In the stirring-deposition method, the Pt nanoparticle suspension was mixed with 50 mL of ethanol containing the appropriate amount of support, followed by continuous stirring at room temperature for 24 h [13]. For the impregnation method, the Pt nanoparticle suspension was dispersed in 10 mL of ethanol together with the zeolite powder. The mixture was stirred at room temperature for 2 h and then heated gradually to 150 °C under constant stirring until complete solvent

evaporation. The resulting dense dark paste was then dried in an oven at 80 °C overnight. This technique was applied exclusively to ZSM-5 with a SiO_2/Al_2O_3 ratio of 80 to enable a direct comparison between the two deposition strategies. The sample was designated as Pt/ZSM-5 (80) imp.

All the catalysts underwent purification to remove residual compounds formed during the nanoparticle synthesis. The solid samples were first dried in air overnight at 60 °C and then dispersed in ethanol. The suspension was vortex-mixed and centrifuged at 5000 rpm for 30 min at room temperature. The supernatant was carefully removed, and the washing cycle was repeated until a neutral pH (~7) was reached. The purified catalysts were then dried at 60 °C to eliminate residual ethanol and moisture.

Finally, two thermal treatments were applied. First, the catalysts were calcined at 350 °C for 12 h (heating rate: 5 °C/min) to remove contaminants and residual organic species. The active metallic platinum phase was then generated by reduction under a mixture of 5% vol H_2 in N_2 (40 mL/min) at 300 °C for 2 h [13].

2.2. Catalyst characterization

Nitrogen adsorption-desorption measurements were performed at −196 °C using a Micromeritics Tristar II 3020 analyzer to determine the textural properties of the materials, including specific surface area, pore-size distribution and pore structure (i.e., microporous vs. mesoporous character). Prior to analysis, the samples were degassed at 200 °C for 2 h under nitrogen flow to remove adsorbed moisture and surface impurities. The specific surface area was calculated according to the Brunauer-Emmett-Teller (BET) model. The total pore volume (V_p) and average pore diameter (D_p) were obtained from the desorption branch of the isotherm using the Barrett–Joyner–Halenda (BJH) method. Micropore volume was further evaluated by applying the t-plot method.

Powder X-ray diffraction (XRD) patterns were acquired using a Philips X'Pert PW3040 diffractometer equipped with Cu Kα radiation (λ = 1.5419 Å). For ZSM-5-based catalysts, measurements were collected in the 2θ range of 5–40°, with a step size of 0.026 ° and a counting time of 56.9 s per step. In contrast, for SBA-15-based catalysts, the 2θ range was set to 0.7–8°, with a step size of 0.013 ° and an acquisition time of 118.3 s per step. Phase identification was performed by comparison with the reference patterns from the International Centre for Diffraction Data (ICDD) Powder Diffraction Files (PDF) database.

Platinum loading was quantified by inductively coupled plasma mass spectrometry (ICP-MS) using a Thermo Scientific iCAP RQ ICP-MS system. Prior to analysis, the catalysts were digested at 200 °C for 40 min in a mixture of nitric acid, hydrochloric acid and hydrogen peroxide. The resulting solutions were subsequently diluted to reach the concentration required for accurate metal determination.

Fourier Transform Infrared (FTIR) spectroscopy measurements were carried out using a Bruker Invenio S spectrometer equipped with a liquid-nitrogen-cooled MCT detector. Spectra were collected in transmittance mode in the 4000–400 cm^{-1} range with a resolution of 2 cm^{-1}. Each spectrum was obtained by averaging 64 scans; background spectra were acquired with 128 scans under identical conditions. The samples were prepared as self-supporting pellets (10–15 mg cm^{-2}) and mounted in a quartz IR cell fitted with optical windows. An initial spectrum was recorded at room temperature, after which the samples were degassed under high vacuum (10^{-4} mbar) and thermally treated at 350 °C for 2 h, before cooling to room temperature. For in situ FTIR experiments, d_3-acetonitrile was used as a probe molecule, following a commonly employed procedure [34,35]. The small size of this molecule facilitates access to acidic sites within the microporous ZSM-5 framework. Its C≡N stretching vibration is also highly sensitive to acid type and strength. Following thermal pretreatment and cooling, the probe molecule was introduced into the cell until a pressure of 20 mbar was reached and maintained for 1 h. Degassing was then performed progressively, first under controlled pressure and then over time. This procedure was continued until the lowest achievable vacuum was reached to evaluate adsorption strength and site distribution.

Carbon monoxide adsorption experiments were performed using the same Bruker Invenio S spectrometer, equipped with a transmission quartz cell adapted for low-temperature measurements. All spectra were acquired under the same instrumental conditions described above. Self-supporting pellets (15–25 mg cm^{-2}) were used for all samples. Prior to CO adsorption, the materials were activated in situ by heating under vacuum (10^{-4} mbar) up to 350 °C (5 °C min^{-1}) and kept at this temperature for 2 h. The samples were then cooled to room temperature under vacuum and subsequently brought to 77 K using liquid nitrogen. CO was introduced stepwise at 77 K, up to calibrated doses and a maximum equilibrium pressure of 20 mbar. Spectra were recorded after each dosing step to follow the evolution of the adsorbed species. After adsorption, the system was progressively evacuated, and spectra were collected during desorption to assess the strength of CO–surface interactions.

Diffuse Reflectance Infrared Fourier Transform Spectroscopy (DRIFTS) experiments were conducted using a Harrick Praying Mantis diffuse reflectance IR cell connected to the same Bruker Invenio S spectrometer. The acquisition parameters were identical to those used in transmission FTIR (4000–400 cm^{-1} range, 2 cm^{-1} resolution). Each spectrum was acquired by averaging 32 scans, while the background was recorded with 256 scans using thermally pretreated KBr (200 °C for 2 h under N_2 flow). DRIFTS experiments were carried out under flowing conditions, using the same gas composition, total flow rate and temperature program used in the catalytic tests.

X-ray photoelectron spectroscopy (XPS) was employed to investigate the chemical state of Pt-based catalysts, with particular focus on the oxidation state of platinum and its interactions with the support. Spectra were recorded using a PHI 5000 Versa Probe II system under the following conditions: bandpass energy of 187.85 eV, take-off angle of 45°, and an X-ray spot size of 100 μm in diameter. The binding energy scale was calibrated using the C 1 s peak at 284.8 eV, as reference.

The morphology, size and spatial distribution of Pt nanoparticles supported on ZSM-5 and silica were examined by transmission electron microscopy (TEM), using a Thermo Scientific Talos F200X microscope equipped with a LaB_6 electron source and operated at an accelerating voltage of 200 kV. For selected samples, a reduced voltage of 80 kV, instead of the standard 200 kV used for the other images, was applied to minimize beam-induced amorphization of the zeolite. Particle size distributions were determined by processing the TEM images using ImageJ software.

Quantitative elemental analysis was performed using Energy Dispersive X-ray Spectroscopy (EDX) to evaluate the elemental composition and Pt distribution within the samples. Since EDX is a local characterization technique, spectra were collected from at least three different regions of each sample, to check that the results were homogeneous and representative. EDX measurements were carried out with an Oxford X-ACT detector mounted on a Zeiss Merlin field emission scanning electron microscope (FESEM) equipped with a Gemini-II column.

NH_3 Temperature-Programmed Desorption (NH_3-TPD) experiments were conducted using an Altamira AMI 300Lite TPDRO system with a thermal conductivity detector (TCD). The measurements were used to evaluate the concentration and strength distribution of the acid sites, which are relevant to VOC oxidation. Approximately 70 mg of catalyst (zeolite or silica-based) was loaded into a quartz U-shaped reactor between two layers of quartz wool and positioned within a tubular furnace. The reactor was pretreated under a He flow (25 mL min^{-1}) at 550 °C for 1 h. After cooling to 100 °C, the catalyst surface was saturated with ammonia by introducing a 10% NH_3/He mixture (40 mL min^{-1}) for 30 min. Physisorbed ammonia was then removed by purging the reactor with pure He (25 mL min^{-1}) for 1 h at 100 °C. Desorption was performed by heating the sample to 600 °C at a rate of 10 °C min^{-1} under He flow (35 mL min^{-1}), followed by a 10 min dwell at the final temperature.

CO chemisorption experiments were conducted on the Pt-based

catalysts using the same apparatus employed for the NH_3-TPD measurements. This technique is widely used for the characterization of supported metal catalysts, as it provides essential information on the accessible metallic surface. Approximately 70 mg of catalyst was loaded into the reactor. Prior to analysis, the samples were pretreated under an argon flow (30 mL min^{-1}) at 50 °C for 5 min to remove residual air. A subsequent reduction step was performed under 5 vol% H_2/Ar. The samples were heated at 10 °C min^{-1} up to 300 °C and maintained at this temperature for 2 h to promote the reduction of PtO_x species to metallic Pt^0. The system was then purged with pure helium (30 mL min^{-1}) for 20 min at 300 °C to remove residual hydrogen. CO chemisorption was carried out at 30 °C under continuous He flow (25 mL min^{-1}). Helium was selected as the carrier gas because its thermal conductivity differs markedly from that of CO. Aliquots of 524 μL of a 10 vol% CO/He mixture were injected every 4 min into the He stream. The outlet concentration was monitored by a thermal conductivity detector (TCD). A total of ten CO pulses were injected for each analysis, and the TCD signal was recorded at an acquisition rate of 0.3 point/s. After completing the adsorption cycle, the system was purged with helium (30 mL min^{-1} for 1 min) and the TCD response was calibrated using five injections of the CO/He mixture.

2.3. Catalytic activity tests

The catalytic oxidation tests were carried out in a fixed-bed quartz reactor with a U-shaped configuration (4 mm inner diameter), housed inside a furnace equipped with PID temperature control. A K-type thermocouple, positioned in direct contact with the catalyst bed, was used to monitor the reaction temperature. The outlet gas composition was continuously analyzed by a non-dispersive infrared (NDIR) gas analyzer (ABB Uras 14).

Prior to reaction, 50 mg of catalyst powder was reduced under a flow of 40 mL min^{-1} of diluted hydrogen (5 vol% H_2 in N_2). The temperature was increased at 5 °C min^{-1} up to 300 °C and maintained for 2 h. This reduction step aimed to convert PtO_x species into metallic platinum (Pt^0) and remove physisorbed contaminants. After reduction, the reactor was cooled to room temperature under a continuous flow of pure nitrogen.

Catalytic tests were conducted by feeding a gas mixture representative of indoor air pollution at a total flow rate of 50 mL min^{-1}. The inlet stream contained 100 ppm of a selected pollutant (CO, ethylene or toluene), 21 vol% O_2 and nitrogen as balance gas. The experiments were terminated upon reaching complete conversion (100%) of the target pollutant. Different heating protocols were adopted depending on the reactivity of the target pollutant. For CO, due to its low-temperature oxidation behaviour, a continuous temperature ramp of 1 °C min^{-1} was applied until complete conversion (100%) was reached. For ethylene, an isothermal stepwise approach was used. The temperature was increased in 5 °C increments with a ramp rate of 2 °C min^{-1} between steps. For toluene, the temperature was raised in 15 °C increments with a ramp rate of 5 °C min^{-1}. Under these experimental conditions, the gas hourly space velocity (GHSV) was 60,000 mL g_{cat}^{-1} h^{-1}. Kinetic analysis was used to evaluate the catalytic behaviour of the samples. Reaction rates were normalized to the Pt content determined by ICP and expressed as mol·h^{-1}·(g of Pt)$^{-1}$.

All experiments were performed under oxygen excess (21 vol%), so the oxygen concentration was considered constant.

3. Results and discussion

3.1. Catalyst textural and structural properties

Tables 1 and 2 summarize the main textural properties of the Pt-based catalysts derived from N_2 physisorption measurements, while the corresponding adsorption-desorption isotherms are reported in Figures S1 and S2 (Supporting Information). When comparing the pure supports with their Pt-loaded materials, no significant loss of surface area was observed. A slightly larger, yet still limited, decrease in specific surface area was observed for the sample prepared by impregnation. This suggests that no substantial pore-blocking phenomena occurred and that the internal surfaces of the supports remained largely accessible. The results in Table 1 confirm the predominantly microporous character of ZSM-5, in agreement with previous reports [36–38]. As shown in Table 2, SBA-15 also retained its mesoporous structure after stirring-deposition of platinum nanoparticles, maintaining an average pore diameter between 5.5 and 7 nm [39]. Table 1 additionally reports the quantified Pt loading. Three samples exhibited Pt contents in line with the theoretical maximum, indicating that stirring deposition can achieve a deposition yield close to 100%. Conversely, the impregnated sample displayed the lowest Pt loading.

Table 1 also reports the Si/Al atomic ratios of the ZSM-5-supported catalysts, calculated from the Si and Al atomic percentages obtained by EDX. For ZSM-5 (50), ZSM-5 (80) and ZSM-5 (117), the measured Si/Al ratios are in agreement with the expected compositions. This confirms that the zeolite frameworks were preserved during catalyst preparation.

Table 2
Textural properties of Pt/SBA-15 and bulk silica determined by nitrogen physisorption and ICP-MS measurements.

Sample	S_{BET}[a] (m^2 g^{-1})	V_{pores}[b] (cm^3 g^{-1})	D_{pores}[c] (nm)	Pt content[d] (wt%)
SBA-15	627	0.75	6.73	-
Pt/SBA-15	612	0.72	6.74	0.68

[a] Surface area obtained via BET method.
[b] Total pore volume evaluated from the nitrogen adsorbed amount at P/P_0= 0.994.
[c] Average pore diameter calculated by BJH (Barrett-Joyner-Halenda) method.
[d] Pt loading obtained through ICP-MS.

Table1
Textural properties of Pt/supports and bulk zeolites determined by nitrogen physisorption and ICP-MS measurements.

Sample	S_{BET}[a] (m^2 g^{-1})	$V_{micropores}$[b] (cm^3 g^{-1})	$S_{micropores}$[b] (cm^3 g^{-1})	V_{pores}[c] (cm^3 g^{-1})	Pt content[d] (wt%)	Atomic ratio (Si/Al)[e]
ZSM-5 SiO_2/Al_2O_3= 50	364	0.108	199	0.26	-	-
Pt/ZSM-5 SiO_2/Al_2O_3= 50	358	0.109	199	0.26	0.67	27
ZSM-5 SiO_2/Al_2O_3= 80	423	0.113	246	0.25	-	-
Pt/ZSM-5 SiO_2/Al_2O_3= 80	406	0.113	232	0.26	0.66	40
Pt/ZSM-5 imp SiO_2/Al_2O_3= 80	383	0.116	236	0.24	0.52	-
ZSM-5 SiO_2/Al_2O_3= 117	332	0.117	219	0.20	-	-
Pt/ZSM-5 SiO_2/Al_2O_3= 117	325	0.111	208	0.20	0.53	56

[a] Surface area obtained by Brunauer-Emmett-Teller (BET) method.
[b] Volume and surface area of micropores evaluated via t-plot method.
[c] Total pore volume evaluated from the adsorbed nitrogen amount at P/P_0= 0.994.
[d] Pt loading obtained through ICP-MS.
[e] Estimated from EDX analysis.

Fig. 1a and Fig. 1b show the powder X-ray diffraction (XRD) patterns of the Pt-supported catalysts, together with those of the corresponding bare supports. All zeolite-based samples display comparable XRD profiles, in agreement with the simulated patterns reported for ZSM-5 [40]. The XRD profiles of zeolites exhibit the characteristic low-angle reflections at 8.14 and 9.04° (2θ) as well as the intense set of peaks in the 23–25° region (e.g. 23.25°, 24.14° and 24.51°), all attributable to the ordered MFI framework [41,42]. The XRD patterns of the parent zeolites exhibit no relevant changes with varying SiO_2/Al_2O_3 ratio, indicating that the overall diffractive features are predominantly governed by the intrinsic framework structure rather than by compositional differences. The sharp and well-defined reflections further confirm the high crystallinity of the supports.

For the Pt/ZSM-5 catalysts (SiO_2/Al_2O_3=50, 80 and 117), no peaks associated with metallic platinum are detected at 2θ= 39.8° and 46.2°, corresponding to the (111) and (200) planes, respectively [43]. This observation is consistent with the low platinum content (**0.5%**wt) and its efficient dispersion, as supported by CO chemisorption measurements. The absence of an extended ordered platinum lattice prevents the detection of platinum diffraction signals [44]. No impurity-related reflections are observed, demonstrating that the structural integrity of the zeolite framework is preserved during the deposition procedure.

Fig. 1b shows the low-angle XRD patterns (2θ range: 0.7–8°) of the SBA-15-based samples. Both profiles exhibit an intense reflection at 2θ ~1°, which can be assigned to the (100) plane of the well-ordered two-dimensional hexagonal mesostructure of SBA-15. The weaker reflections corresponding to the (110) and (200) planes are also visible, confirming the preservation of the ordered mesoporous structure after Pt deposition [45,46].

3.2. Catalyst morphology

3.2.1. Transmission electron microscopy (TEM)

Fig. 2 presents TEM images of Pt nanoparticles (NPs) before and after their deposition onto zeolite and silica supports. The images were acquired at different accelerating voltages to optimise resolution while minimizing beam-induced damage [47]. The polyol reduction method produces small, uniform and nearly spherical Pt NPs, generally below 4 nm, although slightly larger than the 1.9 nm average size reported in the literature under similar synthesis conditions [13]. Particle size distribution analysis (Fig. 2b) yielded an average diameter of approximately 3.2 nm. After deposition by the stirring method, the NP size distribution remained essentially unchanged, with a homogeneous dispersion across the support surface. For ZSM-5, a microporous material, Pt nanoparticles were predominantly located on the external surface. In contrast, impregnation (Fig. 2e) promoted particle coalescence into larger clusters, resulting in a significant decrease in the accessible Pt surface area.

Fig. 2c was acquired at a reduced accelerating voltage (80 kV, compared with the 200 kV used for the other images) to limit beam-induced amorphization of the zeolite. Under these conditions, the ZSM-5 support retained its highly ordered microporous structure, displaying well-defined channels and lattice fringes consistent with preserved crystallinity [48,49]. Finally, Fig. 2h provides a close-up of a single Pt nanoparticle. Lattice fringes with an interplanar spacing of 0.23 nm are observed, corresponding to the (111) crystal plane of metallic platinum [50,51].

As confirmed by N_2 physisorption measurements, SBA-15 exhibits a well-developed mesoporous structure with an average pore diameter of approximately 6 nm. This value is larger than the size of the nanoparticles (≤ 4 nm) obtained via the polyol reduction method. Fig. 3 presents three representative STEM images of the Pt/SBA-15 sample. In Fig. 3a, a significant fraction of Pt NPs is distributed over the external silica surface. However, closer inspection of Figs. 3b and 3c reveals that a portion of the nanoparticles is located along the mesoporous channels of SBA-15. Given their size relative to the pore diameter, these particles may therefore be located inside the channels, which are known to exhibit curvatures [52,53]. This partial insertion of Pt NPs into the curved mesopores may increase contact with silanol (Si-OH) groups, which act as very weak acid sites [54]. These groups are present not only on the external surfaces of the silica grains but also along the pore walls and at intracrystalline defect sites [35].

3.2.2. CO chemisorption

CO chemisorption measurements were carried out to evaluate the metal dispersion, i.e. the fraction of Pt atoms exposed on the catalyst surface relative to the total number of metal atoms in the sample. A stoichiometric factor of 1:1 was applied, assuming that one Pt atom coordinates with one CO molecule [55]. This assumption was validated by CO adsorption at room temperature followed by FT-IR spectroscopy, which revealed a single adsorption band characteristic of linearly adsorbed CO species (see Fig. S3, Supporting Information).

The results of CO chemisorption measurements are summarized in Table 3. High Pt dispersions were obtained for most ZSM-5-supported samples (higher than 57%) and for SBA-15 (72%). In contrast, the sample prepared by impregnation exhibited a markedly lower dispersion (23%), consistent with the formation of the large clusters observed in TEM images. The relatively high dispersion values compared to the

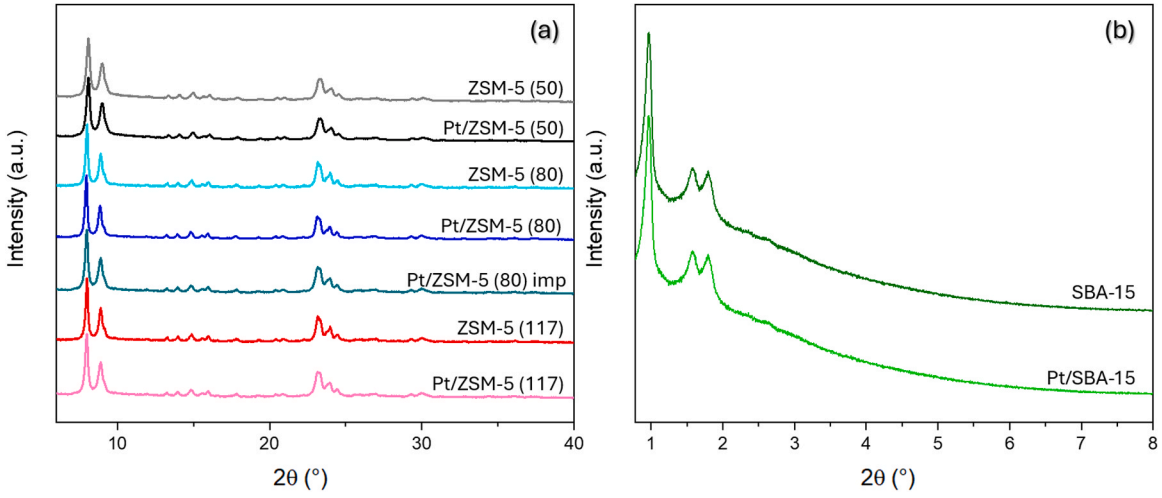

Fig. 1. X-ray diffraction (XRD) profiles of pure ZSM-5 and Pt/ZSM-5 catalysts in the 2θ range of 5–40 ° (a), of pure SBA-15 and Pt/SBA-15 catalysts in the 2θ range of 0.7–8° (b).

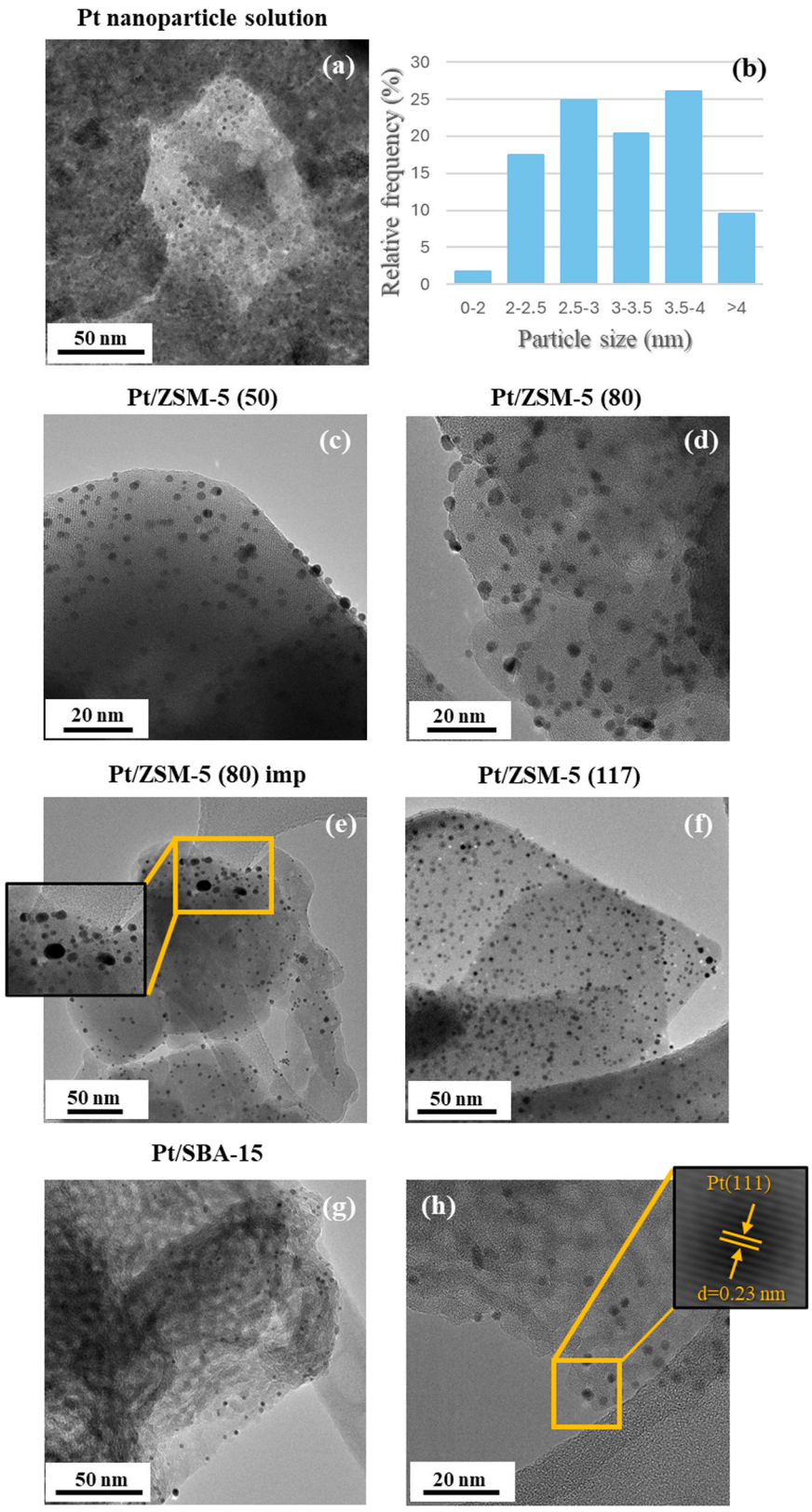

Fig. 2. TEM images of Pt NPs in solution prior to deposition (a), particle size distribution of Pt NPs (b), TEM images of Pt/ZSM-5 (50) (c), Pt/ZSM-5 (80) (d), Pt/ZSM-5 (80) imp (e), Pt/ZSM-5 (117) (f), Pt/SBA-15 (g) and close-up view of a Pt NP showing lattice fringes (h).

average particle sizes observed by TEM (~3 nm) suggest a discrepancy between the two characterization methods. This difference may arise from the distinct information provided by each technique. CO chemisorption selectively probes exposed Pt surface atoms, whereas TEM provides a statistical evaluation of the particles that can be directly visualized. The possible presence of smaller Pt species or sub-nanometric clusters, which are difficult to detect by conventional TEM, cannot be excluded [56]. As shown in Fig. 2b, a fraction of nanoparticles falls in

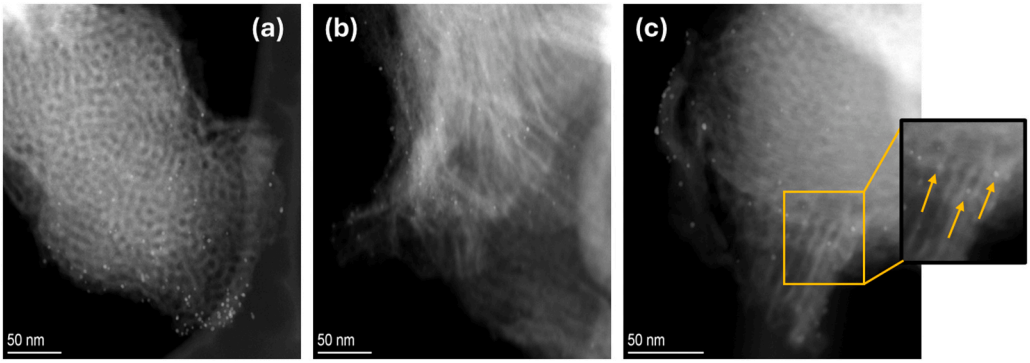

Fig. 3. *STEM images of Pt/SBA-15.*

Table 3
CO chemisorption results for Pt-based catalysts and TEM evaluated particle sizes.

Sample	CO chemisorption		Transmission electron microscopy (TEM)
	Pt dispersion (%)	Pt particles size (nm)	Pt particles size (nm)
Pt colloidal solution	-	-	3.2
Pt/ZSM-5 (50)	67	1.8	3.1
Pt/ZSM-5 (80)	57	2.1	3.2
Pt/ZSM-5 (80) imp	23	5.3	Clusters
Pt/ZSM-5 (117)	76	1.6	3.3
Pt/SBA-15	72	1.7	3.0

the 0–2 nm range and, due to their higher proportion of surface atoms, contributes significantly to the overall dispersion. Notably, SBA-15 exhibited a high dispersion. This result is consistent with its mesoporous structure, which can promote a homogeneous distribution of finely dispersed Pt nanoparticles on both the external surface and within the pore channels.

3.3. Catalyst surface composition and chemical state

Given the fundamental role of platinum in hydrocarbon oxidation, X-ray photoelectron spectroscopy (XPS) was employed to investigate the surface chemical state of the Pt nanoparticles and their interaction with acid or non-acid supports. The Pt 4 f XPS spectra of the Pt-based samples are reported in Figures S4 and S5 (Supporting Information), while the relative amounts of the different Pt species detected for each sample is summarized in Table 4.

In the case of the Pt/ZSM-5 samples, the Pt 4 f spectral windows also included a contribution arising from the Al 2p signal, whose binding energy region extends around 73.9 eV [13,57]. This feature can be attributed to framework Al^{3+} species characteristic of the ZSM-5 structure (see Fig. S4) [48,58,59]. After reduction, the Pt 4 f spectra of all Pt/ZSM-5 catalysts are dominated by a single spin–orbit doublet attributable to metallic platinum. The Pt $4f_{7/2}$ component is centred at approximately 70.5 eV, with the corresponding Pt $4f_{5/2}$ peak located around 73.5 eV, in agreement with values commonly reported for Pt^0 nanoparticles supported on oxide and zeolitic materials [16,38].

Table 4
Surface distribution of Pt oxidation states from XPS analysis for Pt/ZSM-5 zeolites and Pt/SBA-15.

Sample	Pt species	Peak position (eV)		$Pt^0/(Pt^0+Pt^{2+})$ (%)
		4 $f_{7/2}$	4 $f_{5/2}$	
Pt/ZSM-5 (50)	Pt^0	70.6	74.0	100
Pt/ZSM-5 (80)	Pt^0	70.7	74.0	100
Pt/ZSM-5 (80) imp	Pt^0	70.0	73.3	100
Pt/ZSM-5 (117)	Pt^0	70.5	73.8	100
Pt/SBA-15	Pt^0	70.9	74.3	100

XPS analysis shows that, after reduction, platinum is predominantly present as metallic Pt^0 in all catalysts, with no detectable contribution from oxidized Pt species. No significant peak shifts or $Pt^{\delta+}$ species are observed, indicating that strong metal-support interactions or charge-transfer effects are not evident within the limits of XPS detection. Overall, the interaction between Pt nanoparticles and the supports appears to be mainly weak and interfacial in nature.

Conversely, the Pt/SBA-15 sample shows no detectable Al 2p contribution, consistent with the siliceous nature of the SBA-15 framework. The Pt 4 f spectrum also displays only a single metallic Pt doublet, confirming that platinum is fully reduced and present exclusively in the metallic state on the mesoporous silica support. Overall, XPS results demonstrate that the activation treatment leads to effective reduction of Pt species on both zeolitic and mesoporous supports.

3.4. Ammonia temperature-programmed desorption (NH_3-TPD)

NH_3-TPD was employed to evaluate the concentration and strength of acid sites. This technique is sensitive and allows both weak and strong acid sites to be investigated. However, it may overestimate the acidity due to the small size and strong basicity of NH_3 and does not discriminate between site types. NH_3-TPD measurements were not performed on SBA-15 due to its very low acidity, which would not allow a meaningful assessment of acid site distribution.

The NH_3-TPD profiles of the zeolitic supports are shown in Fig. 4. All profiles exhibit a similar behaviour, displaying two main desorption peaks. The first peak, observed at lower temperatures (100–250 °C), can be attributed to weak acid sites, whereas the second peak, appearing at higher temperatures (250–550 °C), corresponds to strong acid sites. Peak deconvolution is summarized in Table 5. The concentrations of both weak and strong acid sites decrease with increasing SiO_2/Al_2O_3 ratio, in agreement with previously reported literature [60,61].

To verify whether the deposition of Pt affects the acidic properties of the supports, NH_3-TPD measurements were also performed on representative Pt-containing samples. No significant differences in total acidity or desorption profiles were observed compared to the bare supports. Therefore, only the acidity data of the parent supports are reported and discussed in the main text, as they can be considered representative of the final catalysts.

3.5. Catalyst surface functional groups

FT-IR spectroscopy was used to investigate the surface functional groups. Since all zeolite samples exhibited very similar spectra, the

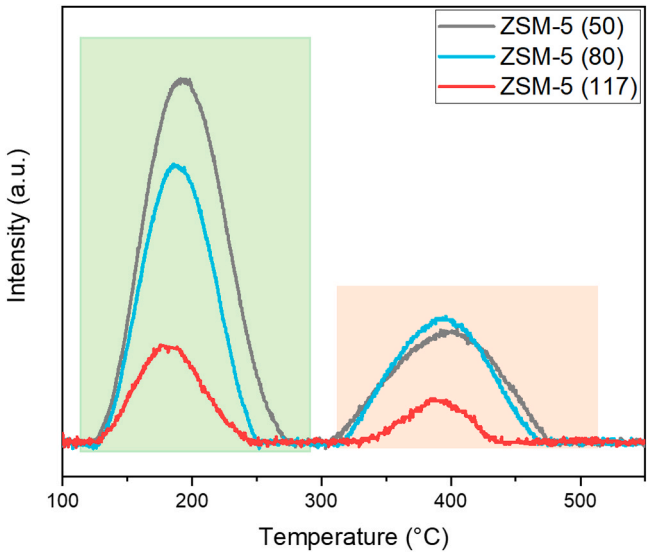

Fig. 4. NH_3 desorption profiles of ZSM-5 supports.

Table 5
NH_3-TPD-derived acid site concentrations.

Sample	Weak acid sites (μmol g_{cat}^{-1})	Strong acid sites (μmol g_{cat}^{-1})	Total acid sites (μmol g_{cat}^{-1})
ZSM-5 (50)	230	145	375
ZSM-5 (80)	153	127	280
ZSM-5 (117)	90	73	163

results obtained for ZSM-5 (117) are shown here as a representative example.

Fig. 5a reports the FT-IR spectrum of the ZSM-5 (117) sample in the OH-stretching region (3800–3200 cm^{-1}) after the thermal pretreatment. This region is particularly informative, as it reflects the nature and distribution of hydroxyl groups associated with different types of acid sites. The spectrum exhibits two main features. A sharp peak at 3746 cm^{-1} is assigned to terminal silanol groups [62]. A distinct absorption peak at around 3613 cm^{-1} is characteristic of bridging hydroxyls of the Si-OH-Al type, corresponding to Brønsted acid sites within the zeolite framework [62,63]. A weak band at around 3675–3670 cm^{-1} is also observed and attributed to OH groups associated with extra-framework aluminium species formed during thermal treatment. For ZSM-5 (117), this band remains very weak, indicating a limited amount of these species [35,64]. In contrast, it is more pronounced for ZSM-5 (50), which has a lower silica to alumina ratio (Figure S7). Overall, the spectrum evidences the coexistence of framework Brønsted acid sites, extra-framework species and defect-related silanol groups in the zeolite.

To further investigate the acid sites of the ZSM-5 zeolites, CD_3CN was employed as a probe molecule for adsorption-desorption experiments. CD_3CN is a small and slightly basic molecule capable of penetrating the zeolite micropores. It was selected for its ability to interact with hydroxyl groups both on the external surface and within the channels. The substitution of hydrogen with deuterium was used to minimize spectroscopic complications related to Fermi resonance [35]. As shown in Fig. 5, the introduction of CD_3CN leads to its adsorption at the hydroxyl sites. The absorption peak at ~3613 cm^{-1}, associated with strong acid sites, was already attenuated at low CD_3CN pressures (6×10^{-1} mbar). An analogous behaviour was observed for the silanol groups. Their band was gradually attenuated at low probe pressures and completely disappeared only at higher pressures (16 mbar), reflecting their weaker acidity and lower reactivity toward the probe molecule.

Additionally, FT-IR spectra collected in the 2350–2250 cm^{-1} region are reported in Fig. 5b for the ZSM-5 (117) sample, while those of the other supports are reported in Fig. S6 (Supporting Information). In this region, bands related to CD_3CN interacting with different acid sites can be observed. Deconvolution of the spectra, summarized in Table 6, indicates that the total number of accessible acid sites increases with decreasing SiO_2/Al_2O_3 ratio. NH_3-TPD measurements, performed on the zeolites and reported in Table 5, confirm this trend. The overall acid site densities are in reasonable agreement with the spectroscopic data. While the quantity of Brønsted acid sites closely follows the aluminium content in the ZSM-5 framework, the weak Lewis acid sites display a different behaviour. In particular, the ZSM-5 (80) sample exhibits the lowest

Table 6
Acid site distribution in zeolite samples determined from CD_3CN adsorption FT-IR.

Sample	LAS[a] (μmol g_{cat}^{-1})	BAS[b] (μmol g_{cat}^{-1})	BAS + LAS (μmol g_{cat}^{-1})	Weak + Strong[c] (μmol g_{cat}^{-1})
ZSM-5 (50)	95	261	356	375
ZSM-5 (80)	10	211	221	280
ZSM-5 (117)	48	122	170	163

[a] Molar extinction coefficient (ε) = 3.60 cm μmol^{-1} [65].
[b] Molar extinction coefficient (ε) = 2.05 cm μmol^{-1} [65]
[c] Evaluated via NH_3-TPD.

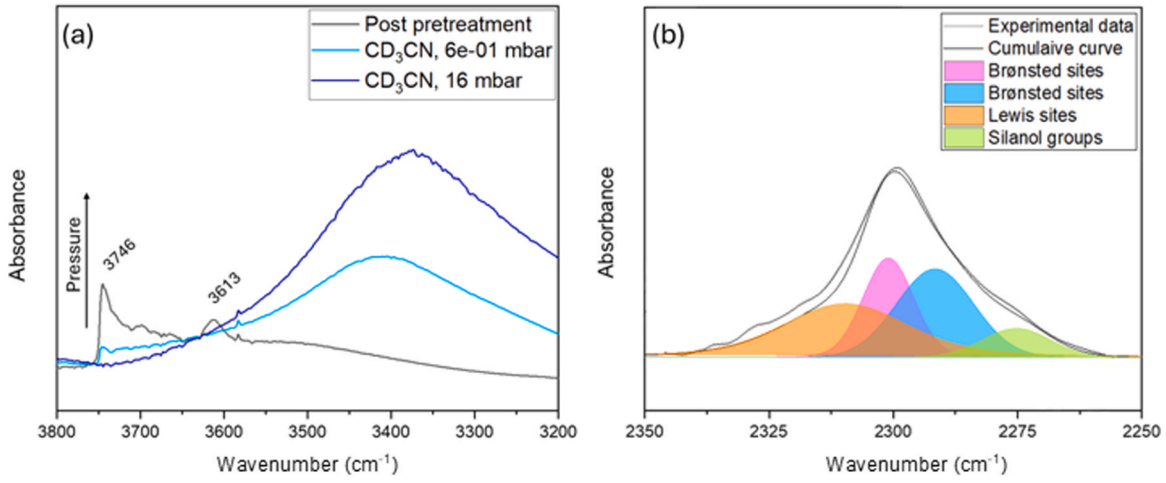

Fig. 5. FT-IR spectra of ZSM-5 (117): (a) OH-stretching region (3800–3200 cm^{-1}) after thermal pretreatment and during CD_3CN adsorption at increasing pressures ($6 \bullet 10^{-1}$ mbar and 16 mbar); (b) C≡N stretching region (2350–2250 cm^{-1}). FT-IR spectra for the other zeolites are reported in Fig. S6.

concentration of weak Lewis sites among the series. These findings highlight that CD_3CN interacts with both strong Brønsted and weak Lewis acid sites, allowing the distribution of acid sites across the zeolite series to be quantified.

3.6. CO adsorption and surface site distribution

CO adsorption FTIR experiments were carried out to further investigate the nature and accessibility of the acid sites identified by CD_3CN measurements [66]. This study was performed at 77 K to stabilise weak adsorption complexes on all the supports, with or without stirring-deposited platinum. Carbon monoxide is a small molecule able to access the zeolite micropores and probe confined environments. Although it is only weakly basic, CO is highly sensitive to the local electronic environment, allowing differentiation between hydroxyl and Lewis-type species. In addition, CO is one of the reactants involved in the studied catalytic reactions, making its adsorption behaviour directly relevant [67,68].

The interaction of CO with surface hydroxyl groups was first examined in the OH stretching region (4000–3000 cm^{-1}). Upon increasing CO pressure, all OH bands progressively shift to lower frequencies, indicating interaction of CO with all the hydroxyl species. A broad feature associated with Brønsted acid sites develops at lower frequencies, while silanol and Al–OH groups also shift, although to a much smaller extent, consistent with weaker interactions. Further details are reported in the Supporting Information (Fig. S7).

The C-O stretching region (2300–2000 cm^{-1}) was then analysed, to gain more detailed insight into the nature of the adsorbed species. For all samples, the spectra were deconvoluted to identify the different contributions. A representative fit of the Pt/ZSM-5 (80) sample is shown in the Supporting Information (Fig. S8), while the complete assignment of the peaks is reported in Table 7.

Several bands can be distinguished, each one associated with a specific type of interaction. At high CO pressure, a main band at ~2138 cm^{-1} is observed and assigned to physisorbed CO confined in the zeolite microporous channels. The structured profile, often appearing as a doublet, is consistent with hindered rotational dynamics and CO-CO interactions. The band reversibly disappears upon evacuation, indicating weak adsorption [62,69]. Additional features observed during subsequent warming, including the formation of carbon dioxide species, are reported in Fig. S9 (Supporting Information). Contributions related to Brønsted acid sites, silanol groups, Al–OH species and extra-framework aluminium (EFAl) are also observed. A further band is assigned to weakly adsorbed or confined CO within the micropores. For Pt-containing samples, an additional band appears between 2120 and 2100 cm^{-1} assigned to CO adsorbed on metallic Pt [74].

Due to the weak and non-stoichiometric interaction of CO with acid sites, the band intensities cannot be directly used to quantify the absolute site concentrations. For this reason, CO-FTIR was only used to evaluate the relative distribution of CO among the different surface functionalities rather than their total amount. The relative contributions were estimated considering only the chemisorbed fraction (Fig. 6).

The percentages are reported for the bare supports, since no significant differences were observed upon Pt deposition. The results show clear differences across the zeolite series. In particular, ZSM-5 (50) and ZSM-5 (117) reveal a higher fraction of CO interacting with EFAl species compared to ZSM-5 (80), in agreement with the lower concentration of Lewis acid sites observed for the latter sample by CD_3CN (Table 6). EFAl species, being electron-poor centres, can induce polarization of the CO molecule [64]. Overall, CD_3CN gives a quantitative measure of acid site density. CO-FTIR reflects how a weak probe molecule distributes across those sites, providing complementary information on surface accessibility and the local environment.

SBA-15, in contrast, mainly shows contributions associated with silanol groups together with a minor fraction of weakly physisorbed CO, consistent with its prevalent mesoporous nature and the absence of framework aluminium and strong acid sites (Fig. S10, Supporting Information) [75].

Table 7
CO vibrational frequencies corresponding to distinct surface adsorption sites.

υ_{CO} (cm^{-1})	Adsorption site
2132–2135	CO physisorbed [62]
2138–2141	CO physisorbed [64,69]
2157–2160	Silanol site (Si-OH) [70]
2165–2169	Al-OH [71,72]
2173–2174	Brønsted acid sited [67,72]
2186–2189	Extraframework Al (EFAl) [72,73]

3.7. Catalytic activity tests

The impregnated sample showed lower Pt dispersion, as confirmed by TEM and CO chemisorption results. Therefore, only catalysts prepared by the stirring-assisted method were selected for the VOC oxidation tests. The catalytic activity of the Pt-based samples was first evaluated using CO oxidation as a model reaction. This probe reaction was used to evaluate the ability of Pt sites to activate oxygen and promote oxidation under mild conditions. The results for Pt/ZSM-5 catalysts with different SiO_2/Al_2O_3 ratios and for Pt/SBA-15 are shown in Fig. 7. The corresponding T_{10}, T_{50} and T_{90} values are reported in Table 8 and represent the temperatures required to reach 10%, 50% and 90% CO conversion, respectively. Despite the low Pt loading, CO oxidation occurs at very low temperatures, achieving complete conversion below 55 °C. Among the tested samples, Pt/ZSM-5 with SiO_2/Al_2O_3 ratios of 50 and 117 exhibited the highest activity, displaying nearly identical conversion profiles. The remaining two samples also showed comparable curves. Significantly, partial CO conversion (approximately 4–8%) occurs even at room temperature, indicating that the reaction proceeds without additional heating. Despite the high Pt dispersion on SBA-15, CO oxidation is slightly less efficient than on Pt/ZSM-5, highlighting a contribution from the support. The reliability of the CO oxidation measurements was verified by repeating selected catalytic tests under identical conditions, yielding highly consistent conversion curves (see Fig. S11 and Fig. S12, Supporting Information). XPS, performed on the spent catalysts after CO oxidation, confirms that Pt remains fully metallic on both zeolite and mesoporous supports (Fig. S13, Supporting Information). To verify that the preservation of the metallic Pt phase translated into stable catalytic performance, repeated CO oxidation cycles were carried out, showing highly reproducible conversion profiles (Fig. S14, Supporting Information).

In H^+-ZSM-5, most Brønsted acid sites are located within the zeolite channels, where they are generally not in close proximity to the Pt nanoparticles on the external surface, except a small fraction present at the pore mouths [64,76,77]. In contrast, Lewis acid sites, particularly those associated with extra-framework Al species (EFAl), can be present in more accessible positions, such as pore mouths or external surface regions. These sites are therefore more likely to interact with CO molecules and to be located closer to the supported Pt nanoparticles [35,77]. Moreover, extra-framework species are generally associated with stronger interactions compared to framework-related ones [70].

Low-temperature ^{13}C solid-state NMR studies on CO adsorbed on zeolites by Yakimon et al. (2021) [78] have shown that CO can interact weakly and dynamically with Lewis acid sites, without forming stable complexes. Although these interactions are relatively weak, they can induce a slight polarization of the CO molecule. In the present system, this effect may become relevant when Lewis sites are located near Pt nanoparticles.

The results obtained indicate that Pt nanoparticles are the primary active phase for CO oxidation, while the zeolite support may contribute to the differences observed at low temperature. Pt/ZSM-5 (50) and Pt/ZSM-5 (117), which show the highest Pt dispersions, exhibit the best

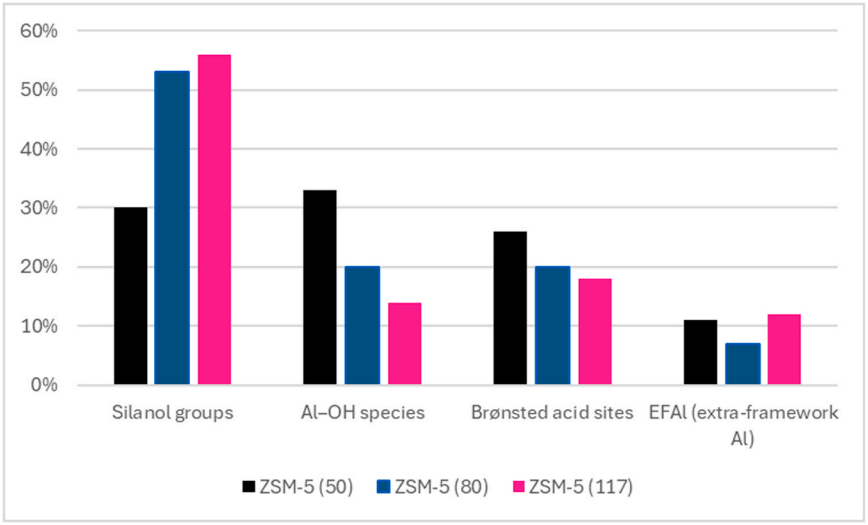

Fig. 6. Qualitative distribution of chemisorbed CO over zeolite sites obtained from FTIR band deconvolution.

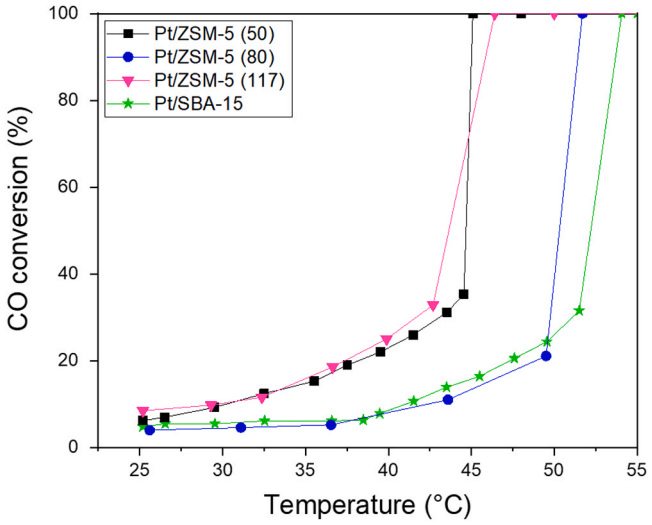

Fig. 7. CO oxidation profiles of Pt/ZSM-5 (SiO_2/Al_2O_3= 50, 80 and 117, prepared by stirring method) and Pt/SBA-15. Reaction conditions: 100 ppm CO, 21% O_2, balance N_2, total flow = 50 mL min^{-1}.

Table 8
Temperatures corresponding to 10% (T_{10}), 50% (T_{50}) and 90% (T_{90}) CO conversion for Pt/ZSM-5 and Pt/SBA-15 catalysts. The table also reports the corresponding turnover frequencies (TOFs) and the ratio between the densitiy of EFAl Lewis acid sites and the density of exposed Pt atoms.

Sample	T_{10} (°C)	T_{50} (°C)	T_{90} (°C)	TOF[a] (x 10^{-4}) s^{-1}	Specific reaction rate[a] (mol_{CO} h^{-1} g_{Pt}^{-1})	EFAl/Pt^0 ratio[b]
Pt/ZSM-5 (50)	30.2	44.7	45.0	7.3	$8.3 \bullet 10^{-3}$	1.11
Pt/ZSM-5 (80)	42.4	50.3	51.4	3.0	$3.0 \bullet 10^{-3}$	0.14
Pt/ZSM-5 (117)	29.7	43.6	45.9	8.3	$1.1 \bullet 10^{-2}$	1.07
Pt/SBA-15	41.0	52.2	53.7	2.5	$2.0 \bullet 10^{-3}$	-

[a] values determined from the CO conversion recorded at 40 °C.
[b] The EFAl/Pt ratio was calculated as the density of extra-framework Lewis acid sites divided by the density of exposed Pt atoms.

CO oxidation performance. Pt/ZSM-5 (80), characterized by the lowest Pt dispersion, has lower activity. The differences in catalytic behaviour therefore do not seem to be directly correlated to acidity alone. At the same time, the higher fraction of CO interacting with EFAl species observed for the most active Pt/ZSM-5 samples (i.e. those with SiO_2/Al_2O_3 = 50 and 117) is compatible with a possible promotional effect of accessible Lewis acid sites, which may weakly polarize the CO molecule and facilitate its activation near Pt nanoparticles. Nevertheless, the significance of the contribution of EFAl sites cannot be separated from the one of Pt dispersion. Pt/SBA-15 is slightly less active than the best ZSM-5-based samples, despite its relatively high Pt dispersion, further indicating that support-dependent effects may contribute to the observed catalytic behaviour. Overall, CO oxidation appears to be primarily governed by exposed metallic Pt sites, with Pt dispersion and the local environment provided by the support contributing to the differences among the catalysts.

Turnover frequencies (TOFs) and normalized reaction rates, calculated for all the samples, are reported in Table 8. Apparent TOF values were estimated by normalizing the rates to the amount of exposed Pt surface atoms derived from chemisorption measurements. These values do not account for the contribution of acid sites. Reaction rates were normalized to the Pt content determined by ICP analysis and expressed as mol_{CO} h^{-1} g_{Pt}^{-1}. Although the TOFs measured under low CO concentration (100 ppm) and low-temperature conditions are relatively low (on the order of 10^{-4} s^{-1}), they follow trends consistent with those reported in the literature for similar Pt-based catalysts under higher CO partial pressures [53,66]. Among the Pt/ZSM-5 catalysts, Pt/ZSM-5 (50) and Pt/ZSM-5 (117) exhibit the highest TOFs (4.4×10^{-4} s^{-1} and 4.3×10^{-4} s^{-1}, respectively), while Pt/ZSM-5 (80) and Pt/SBA-15 show the lowest TOFs (1.8×10^{-4} s^{-1}). A similar trend is observed for the normalized reaction rates. This suggests that the differences in catalytic activity cannot be attributed only to variations in Pt metallic phase, since Pt particle size and dispersion are relatively comparable among the samples. Table 8 also reports the ratio between accessible extra-framework Al species, estimated from FT-IR analysis, and exposed Pt atoms. Pt/ZSM-5 (50) and Pt/ZSM-5 (117) display higher EFAl/Pt ratios than Pt/ZSM-5 (80), suggesting that the local environment surrounding Pt nanoparticles differs among the catalysts. The presence of nearby Lewis acidic species may still influence CO adsorption and activation through weak local interactions under low-temperature conditions [78].

For both ethylene and toluene oxidation, the catalytic performance was evaluated on the basis of CO_2 formation, taken as an indicator of conversion. The catalytic performance of the Pt-based catalysts in

ethylene oxidation is reported in Fig. 8 as CO_2 yield versus temperature. CO_2 production was first detected at approximately 30–35 °C, with all samples showing comparable initial activity. Pt/ZSM-5 catalysts prepared by stirring exhibited nearly overlapping conversion profiles, reaching complete ethylene oxidation below 80 °C, whereas mesoporous Pt/SBA-15 displayed lower CO_2 yields over the same temperature range.

Only minor differences in catalytic performance were observed among the ZSM-5 catalysts despite their different silica to alumina ratios. This indicates that the overall activity is not directly governed by the total concentration of Brønsted acid sites. This observation is consistent with the apparent TOF values and normalized reaction rates reported in Table 9, which are very similar for all Pt/ZSM-5 catalysts. In contrast, Pt/SBA-15 exhibits lower reaction rates, suggesting that support properties influence the catalytic behaviour beyond the contribution of the metallic phase alone.

At low temperatures (<60 °C), all catalysts show comparable activities, indicating that ethylene oxidation is mainly controlled by exposed Pt sites. At higher temperatures, differences between Pt/ZSM-5 and Pt/SBA-15 become more evident. As shown in Figure S16 (Supporting Information), ethylene interacts more strongly with the zeolitic supports than with SBA-15. Brønsted acid sites are known to interact with and protonate olefinic molecules. They may therefore contribute to ethylene adsorption and activation. However, the similar ethylene oxidation performance of the three Pt/ZSM-5 catalysts, despite their different acid site densities, indicates that the total concentration of Brønsted acid sites does not directly control their catalytic activity. The microporous architecture of ZSM-5 may also favour local enrichment and confinement of ethylene in the proximity of the active Pt sites. Since ZSM-5 and SBA-15 differ in both acidity and pore architecture, these effects cannot be clearly separated. The enhanced performance of Pt/ZSM-5 may therefore result from the combined effects of Brønsted acidity, adsorption properties and microporous architecture, while metallic Pt sites primarily govern the oxidation reaction itself. This interpretation is consistent with the XPS and CO-FTIR results, which do not indicate significant electronic metal–support interactions or charge-transfer effects.

The stability of the catalysts was further evaluated by a time-on-stream (TOS) experiment (Figure S15, Supporting Information). This experiment also provides insight into the influence of water formed during the reaction.

The catalytic performance of the samples in toluene oxidation is shown in Fig. 9. Temperatures corresponding to 10% (T_{10}), 50% (T_{50}) and 90% (T_{90}) CO_2 yield are reported in Table 10. Apparent TOF values were conservatively estimated based on exposed Pt atoms, for the same reasons discussed above for ethylene oxidation. CO_2 formation begins to be detected around 80 °C for all catalysts, with yields below 2%. However, clear differences in catalytic behaviour emerge already at the onset of toluene oxidation. The three Pt/ZSM-5 catalysts prepared by the stirring method exhibit nearly identical conversion profiles. Complete toluene oxidation is reached at approximately 140 °C. In contrast, Pt/SBA-15 shows a delayed oxidation onset and lower activity, reaching complete conversion only at around 180 °C.

Compared with ethylene, toluene oxidation requires higher temperatures because of the greater stability of the aromatic molecule. The three Pt/ZSM-5 catalysts show similar activity despite their different acid site densities. This indicates that the total concentration of acid sites does not directly control the catalytic performance. However, Brønsted acid sites may still promote toluene adsorption and activation. Consistently, Pt/SBA-15 shows significantly lower activity, suggesting a favourable role of the zeolitic support. Since ZSM-5 and SBA-15 differ in both acidity and pore architecture, these effects cannot be clearly separated. The higher activity of Pt/ZSM-5 may therefore result from the combined effects of Brønsted acidity, adsorption properties and microporous architecture on toluene adsorption and on the behaviour of reaction intermediates.

Table 9
Temperatures corresponding to 10% (T_{10}), 50% (T_{50}) and 90% (T_{90}) C_2H_4 yield for Pt/ZSM-5 and Pt/SBA-15 catalysts during ethylene oxidation. The table also reports the corresponding turnover frequencies (TOFs).

Sample	T_{10} (°C)	T_{50} (°C)	T_{90} (°C)	TOF[a] (x 10^{-4}) s^{-1}	Specific reaction rate[a] (mol_{C2H4} h^{-1} g_{Pt}^{-1})
Pt/ZSM-5 (50)	41.3	57.0	68.1	8.6	$4.6 \bullet 10^{-3}$
Pt/ZSM-5 (80)	39.4	57.7	72.2	8.9	$4.5 \bullet 10^{-3}$
Pt/ZSM-5 (117)	44.6	59.8	72.6	6.8	$4.6 \bullet 10^{-2}$
Pt/SBA-15	41.6	68.8	89.9	5.5	$1.6 \bullet 10^{-3}$

[a] values determined from the ethylene conversion recorded at 50 °C.

3.8. Catalytic kinetics

To further investigate the catalytic behaviour of the Pt-based

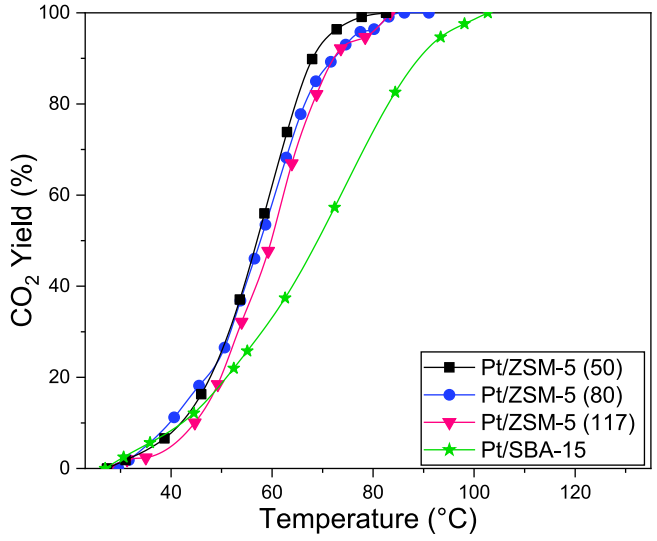

Fig. 8. C_2H_4 oxidation profiles of Pt/ZSM-5 (SiO_2/Al_2O_3= 50, 80 and 117, prepared by stirring method) and Pt/SBA-15. Reaction conditions: 100 ppm C_2H_4, 21% O_2, balance N_2, total flow= 50 mL min^{-1}.

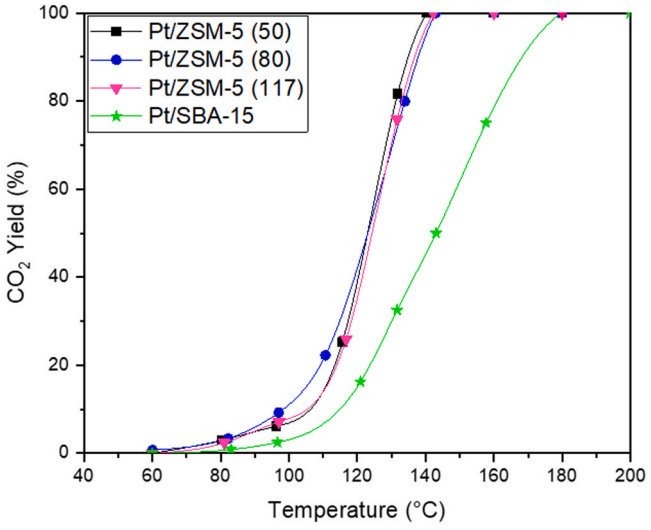

Fig. 9. C_7H_8 oxidation profiles of Pt/ZSM-5 (SiO_2/Al_2O_3= 50, 80 and 117, prepared by stirring) and Pt/SBA-15. Reaction conditions: 100 ppm C_7H_8, 21% O_2, balance N_2, total flow= 50 mL min^{-1}.

Table 10
Temperatures corresponding to 10% (T_{10}), 50% (T_{50}) and 90% (T_{90}) C_7H_8 yield for Pt/ZSM-5 and Pt/SBA-15 catalysts during oxidation. The table also reports the corresponding turnover frequencies (TOFs)..

Sample	T_{10} (°C)	T_{50} (°C)	T_{90} (°C)	TOF[a] (x 10^{-4}) s^{-1}	Specific reaction rate[a] (mol_{C7H8} h^{-1} g_{Pt}^{-1})
Pt/ZSM-5 (50)	100.1	122.7	135.6	3.1	$9.9•10^{-3}$
Pt/ZSM-5 (80)	97.8	121.8	138.4	4.3	$9.5•10^{-3}$
Pt/ZSM-5 (117)	100.0	123.9	137.9	3.2	$9.4•10^{-2}$
Pt/SBA-15	115.3	143.1	168.1	1.3	$6.8•10^{-3}$

[a] values determined from the toluene conversion recorded at 100 °C.

catalysts, a kinetic analysis was performed by estimating the apparent activation energies (E_a) from Arrhenius plots. The reaction rates measured during CO, ethylene and toluene oxidation were fitted according to the Arrhenius equation. Here, (r) is the reaction rate expressed in [$\mu mol \cdot g_{Pt}^{-1} \cdot s^{-1}$] and (T) is the absolute temperature [K]. The corresponding Arrhenius plots are reported in Fig. 10, with the calculated activation energies.

The activation energies were calculated using only data points corresponding to conversions below approximately 25%. This range was selected to minimize the influence of mass-transfer limitations and changes in reactant concentration along the catalyst bed [79]. Apparent activation energies were obtained from the slopes of the Arrhenius plots using reaction rates normalized to the Pt content. In all cases, the determination coefficient (R^2) was close to unity, indicating a satisfactory fit of the experimental data.

For CO oxidation, Pt/ZSM-5 (117) exhibited the lowest apparent activation energy (60 kJ mol^{-1}), followed by Pt/SBA-15 (68 kJ mol^{-1}) and Pt/ZSM-5 (80) (74 kJ mol^{-1}). This trend is consistent with the catalytic activity observed in the light-off experiments and may reflect the combined influence of Pt dispersion and the local environment provided by the support. Since CO is only weakly adsorbed on the supports, the reaction appears to be mainly governed by the properties of the metallic Pt active sites.

In contrast, all catalysts exhibited similar activation energies for ethylene oxidation, ranging from 106 to 113 kJ mol^{-1}. Despite the lower activity observed for Pt/SBA-15 in the light-off curves, its activation energy remained comparable to those measured for Pt/ZSM-5 catalysts. This result suggests that the intrinsic oxidation pathway is largely controlled by the Pt active sites. Consistently, all catalysts displayed similar activities below approximately 60 °C. At higher temperatures, however, Pt/ZSM-5 catalysts became more active than Pt/SBA-15. This suggests that the zeolitic support promotes ethylene adsorption and increases its local concentration near the Pt nanoparticles. The support therefore appears to affect adsorption rather than substantially modifying the apparent reaction barrier.

A more pronounced support effect was observed for toluene oxidation. Pt/ZSM-5 (50), Pt/ZSM-5 (117) and Pt/ZSM-5 (80) exhibited similar activation energies (from 70 to 77 kJ mol^{-1}), whereas Pt/SBA-15 showed a significantly higher value (92 kJ mol^{-1}). Unlike ethylene, the influence of the support is already evident within the low-conversion region used for the kinetic analysis. This indicates a stronger involvement of the zeolitic environment in the adsorption and activation of the aromatic molecule. The lower activation energies observed for the zeolite-supported catalysts are consistent with the stronger interaction of toluene with the acidic zeolitic framework and with the enhanced catalytic activity observed in the light-off experiments.

Overall, the kinetic analysis confirms that Pt nanoparticles constitute the primary active phase for oxidation, particularly at low temperature. The role of the support becomes increasingly important for VOC oxidation and depends on the nature of the reactant. Ethylene oxidation appears to be mainly controlled by Pt active sites at low temperature, with the support primarily affecting adsorption. In contrast, toluene oxidation is more strongly influenced by the zeolitic environment, even in the low-conversion region. This contribution is reflected in the lower apparent activation energies and higher catalytic activity of Pt/ZSM-5.

3.9. Comparison with literature data

The catalytic performance of the present materials was compared with representative Pt-based catalysts reported in the literature for toluene oxidation. Pt/ZSM-5 (50) was selected as representative of the ZSM-5 catalysts, since the three samples showed similar catalytic performance despite their different acid site densities. Studies performed at 100 ppm toluene were preferentially selected. Pt loading, catalyst mass and space velocity were included to account for differences in reaction conditions (Table 11).

The selected literature catalysts include Pt supported on CeO_2, CuO–Fe_3O_4 (CFO), microporous silica (MS) and ZSM-5. Among the catalysts tested at 100 ppm toluene, Pt(EG)@CeO_2 shows the lowest T_{50} and T_{90}. The present Pt/ZSM-5 catalyst also shows good low-temperature activity with a similar Pt loading. Its T_{90} of 136 °C is close to that of Pt(EG)@CeO_2 (130 °C), despite the higher space velocity used in the test. It is also lower than those reported for Pt/CuO–Fe_3O_4 and Pt/MS at the same toluene concentration and space velocity. The relatively high Pt dispersion of the present Pt/ZSM-5 catalysts may also contribute to their good activity at low Pt loading. An analogous Pt/ZSM-5 catalyst from literature was also included in Table 11, despite it was tested with 1000 ppm of toluene while the present work focuses on low, indoor-relevant concentrations of VOCs. Differences in toluene

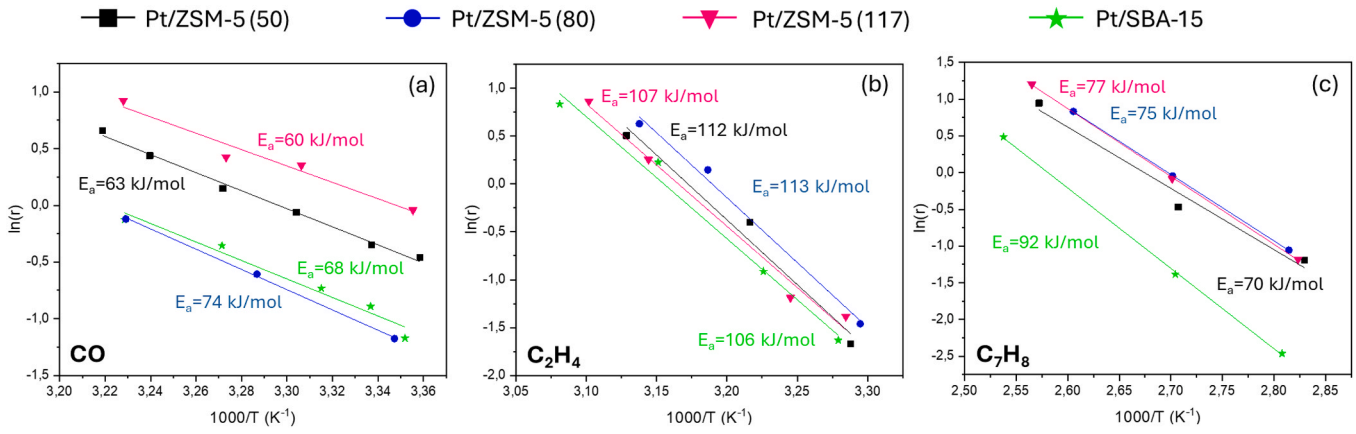

Fig. 10. Arrhenius plots for (a) CO oxidation, (b) ethylene oxidation and (c) toluene oxidation over Pt/ZSM-5 (50), Pt/ZSM-5 (80), Pt/ZSM-5 (117) and Pt/SBA-15 catalysts. Solid lines correspond to linear fits used for the calculation of the apparent activation energies.

Table 11
Comparison of the catalytic performance of the present Pt/ZSM-5 (50) sample with the ones of representative Pt-based catalysts for toluene oxidation described in the literature.

Catalysts	Pt loading (wt%)	Catalyst mass (mg)	Toluene (ppm)	Space velocity (mL g^{-1} h^{-1})	T_{50} (°C)	T_{90} (°C)	Reference
Pt/ZSM-5 (50)	0.67	50	100	60,000	123	136	This work
Pt(EG)@CeO_2	0.44	200	100	24,000	116	130	[80]
Pt/CuO-Fe_3O_4	0.50	100	100	60,000	168	185	[81]
Pt/MS	2.0	100	100	60,000	< 140[a]	149	[82]
Pt/ZSM-5 (Si/Al=46)	0.50	200	1000	12,000	166	177	[83]

[a] Estimated from the reported light-off curve.

concentration, catalyst mass and space velocity should therefore be considered when comparing T_{50} and T_{90} values.

3.10. DRIFTS study of catalytic mechanism

The behaviour of Pt/ZSM-5 (117) under toluene oxidation conditions was further investigated by DRIFTS. The same reaction conditions used for catalytic toluene oxidation were applied. Upon the introduction of toluene at 60 °C (Fig. 11), characteristic FT-IR bands appear in different spectral regions. In the low-frequency region, peaks at 740 and 696 cm^{-1} correspond to out-of-plane bending of C-H bonds in mono-substituted aromatic rings (Fig. 11a) [84]. In the 1650–1450 cm^{-1} region, two peaks are assigned to C=C skeletal vibrations of the aromatic ring (Fig. 11b) [85–87]. In the 3000–2800 cm^{-1} region, the bands at 3088, 3064 and 3028 cm^{-1} are associated with aromatic C-H stretching. The bands at 2930 cm^{-1} and 2874 cm^{-1} correspond to asymmetric and symmetric C-H stretching of the methyl group, respectively, and are indicative of physically adsorbed toluene (Fig. 11c) [36,85,88]. Upon toluene exposure, changes are observed in the OH stretching region. The band associated with isolated hydroxyl groups around 3700 cm^{-1} decreases in intensity, while a broad shoulder develops at lower wavenumbers. This behaviour suggests hydrogen-bonding interactions between adsorbed toluene molecules and surface hydroxyl groups, including Brønsted acid sites (Fig. 11d) [36].

As shown in Fig. 12a, the Pt/ZSM-5 (117) sample was heated up to 160 °C, using the same gas composition and temperature ramp adopted during the catalytic tests. Upon heating, a new band near 1770 cm^{-1} appeared at 140 °C. This band is assigned to the asymmetric C=O stretch of cyclic unsaturated anhydrides, commonly associated with the oxidation of benzoic acid-type intermediates [85,89].

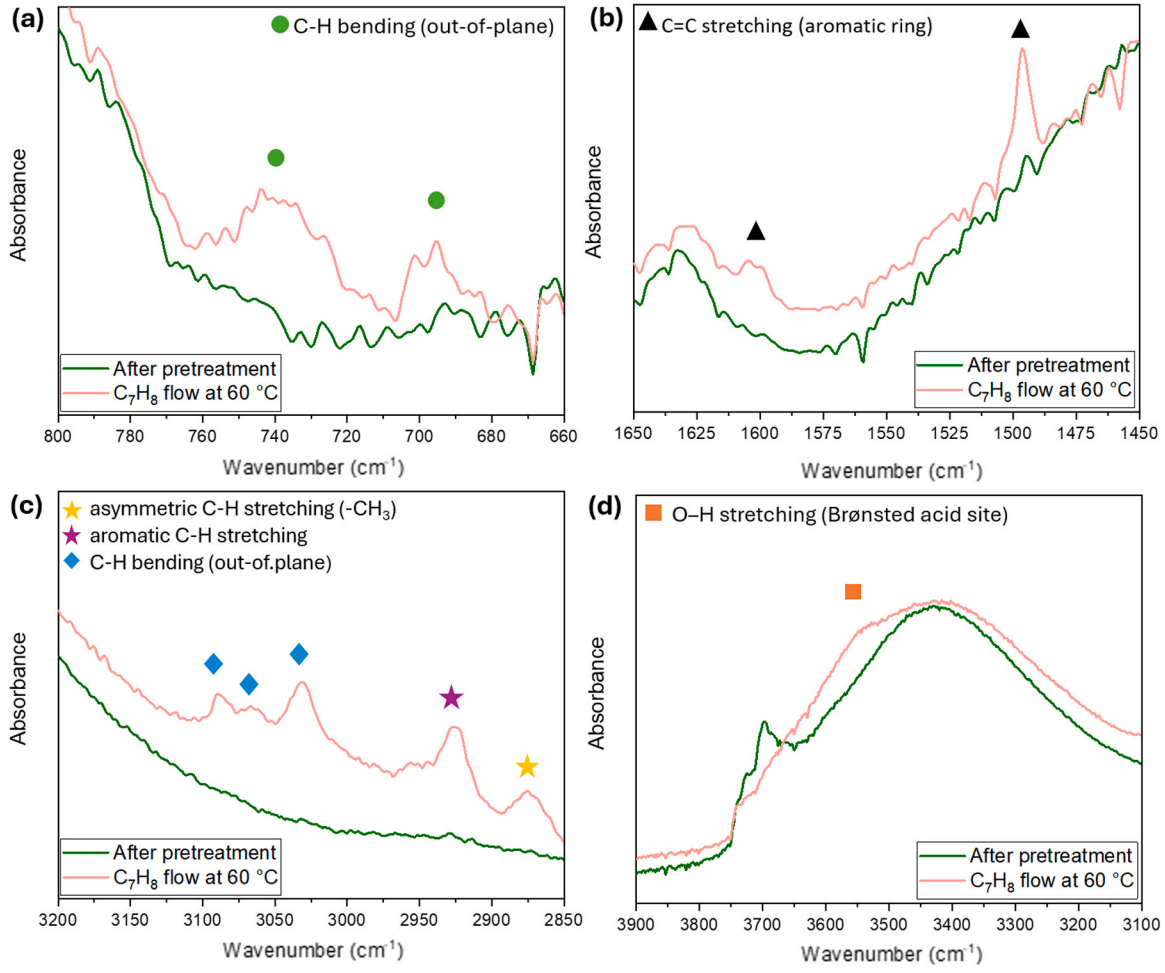

Fig. 11. DRIFTS spectra of Pt/ZSM-5 (117) under toluene oxidation conditions: comparison between the pre-treated catalyst (green) and the same sample after exposure to toluene at 60 °C (pink). Four spectral regions are reported: 800–660 cm^{-1} (a), 1650–1450 cm^{-1} (b), 3200–2850 cm^{-1} (c) and 3900–3100 cm^{-1} (d).

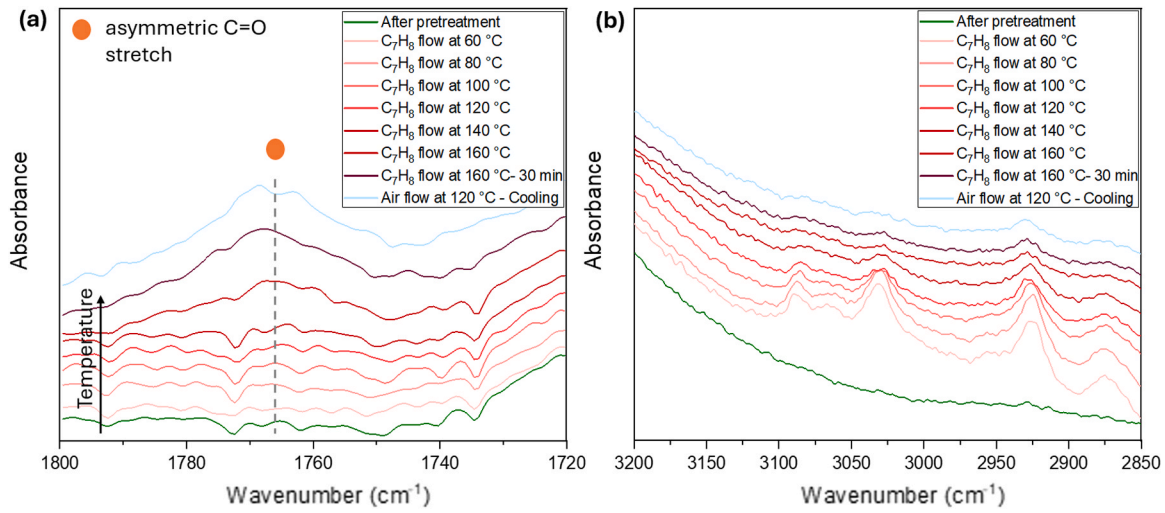

Fig. 12. DRIFTS spectra of Pt/ZSM-5 (117) during heating up to 160 °C and cooled at 120 °C with air, reproducing the temperature ramp applied in the toluene oxidation reactor. Spectral regions: 1800–1720 cm^{-1} (a) and 3200–2850 cm^{-1} (b).

The persistence of this band during the experiment indicates the accumulation of oxidized surface species within the zeolite micropores and under reaction conditions. This "trapping effect" is consistent with the colour change observed for the catalyst after reaction. The temporary retention of these intermediates does not prevent complete oxidation, which is achieved below 150 °C. In contrast, Pt/SBA-15 with its larger mesopores and lower surface acidity, did not show any evident colour variation after reaction.

Cooling the sample under air (Fig. 12b) results in a decrease in the intensity of the 3200–2850 cm^{-1} region. This indicates the continued consumption of adsorbed toluene-derived species. Low-intensity residual bands suggest that a small fraction of adsorbates remained on the catalyst surface. The anhydride-related band remained detectable during cooling, confirming the persistence of these oxidized species under the experimental conditions. No distinct CO_2 infrared band was observed, likely because of its rapid desorption and removal by the carrier gas.

It should be noted that the DRIFTS signals are relatively weak because the experiments were performed using only 100 ppm. This concentration was selected to reproduce the conditions during the catalytic tests.

4. Conclusions

In summary, 0.5 wt% Pt catalysts supported on microporous ZSM-5 zeolites with different SiO_2/Al_2O_3 molar ratios and on mesoporous SBA-15 were prepared via stirring-assisted deposition and conventional impregnation. The stirring-assisted method yielded well-dispersed and reproducible Pt nanoparticles while preserving the structural properties of the supports. The method also showed good reproducibility, enabling a consistent assessment of support effects. Conventional impregnation led to broader particle size distributions and lower metal dispersion. Therefore, these catalysts were not further considered for catalytic evaluation.

XPS and CO-FTIR analyses indicate that Pt is mainly present in the metallic state after reduction, with no clear evidence of strong electronic metal–support interactions or significant charge transfer. Pt nanoparticles are predominantly located on the external surface of ZSM-5, while partial insertion into SBA-15 mesopores cannot be excluded.

The support affects the local environment around the metal particles. CO oxidation is primarily governed by exposed Pt sites, although Pt dispersion and the local environment provided by the support may contribute to the observed activity. By contrast, ethylene and toluene oxidation show comparable activities across ZSM-5 samples despite their different molar SiO_2/Al_2O_3 ratios. This indicates that the total concentration of Brønsted acid sites does not directly control the catalytic performance under the investigated conditions. The zeolite framework can nevertheless contribute through adsorption-related effects and the creation of a favourable local environment for the reactants, while the oxidation reaction itself predominantly occurs on metallic Pt sites.

Compared with SBA-15, Pt/ZSM-5 shows higher VOC oxidation activity. This behaviour may result from the combined effects of acidity, adsorption properties and microporous architecture, including confinement effects. However, the similar performance of the three ZSM-5 catalysts despite their different acid site densities indicates that acidity alone does not determine VOC oxidation activity. Since ZSM-5 and SBA-15 differ in both acidity and pore architecture, the contribution of each factor cannot be clearly distinguished from the present results. DRIFTS results further suggest that oxidized intermediates formed during toluene oxidation can be temporarily retained within the zeolite framework, which may favour their further transformation.

Overall, this study shows that the catalytic behaviour of low-loading Pt catalysts for VOC oxidation is governed by the interplay between exposed metallic Pt sites and the physicochemical properties of the support. By maintaining comparable Pt nanoparticle characteristics across the investigated catalysts, the contribution of the support could be more clearly distinguished. Electronic metal-support interactions do not appear to play a significant role. Instead, pore architecture, adsorption properties and the local environment surrounding Pt can influence catalytic performance even when the metallic phase remains essentially unchanged. In particular, the results indicate that total Brønsted acidity alone is not a sufficient descriptor of VOC oxidation activity. Confinement and adsorption effects associated with the zeolite framework can instead promote reactant availability and intermediate transformation near the active Pt sites. Besides demonstrating activity at only 0.5 wt% Pt and under indoor-relevant VOC concentrations (100 ppm), these findings provide new insight into the role of zeolitic supports in Pt-catalysed VOC oxidation and suggest that future catalyst design should focus not only on Pt dispersion and acidity, but also on controlling pore accessibility and the local environment of the metal sites.

CRediT authorship contribution statement

Alessia Cometto: Writing – review & editing, Writing – original draft, Methodology, Investigation, Formal analysis, Data curation. **Enrico Sartoretti:** Writing – review & editing, Supervision,

Methodology, Investigation, Formal analysis, Conceptualization. **Samir Bensaid:** Writing – review & editing, Supervision, Resources, Formal analysis, Conceptualization. **Nunzio Russo:** Writing – review & editing, Supervision, Resources, Formal analysis, Conceptualization.

Declaration of Generative AI and AI-assisted technologies in the writing process

During the manuscript preparation, the authors used ChatGPT (OpenAI) in order to assist with language editing and text refinement. After using this service, the authors reviewed and edited the content as needed and take full responsibility for the content of the published article.

Declaration of Competing Interest

The authors declare that they have no known competing financial interests or personal relationships that could have appeared to influence the work reported in this paper.

Acknowledgments

The authors thank Camilla Galletti and Marco Allione for performing XRD and TEM measurements. Federica Beraudo and Pietro Gaudio are also kindly acknowledged for helping collect data during their MS thesis preparations. The authors acknowledge the funding received by the Italian Ministero dell'Università e della Ricerca (MUR) under the Dipartimento di Eccellenza 2018–2022 program and the PON Ricerca e Innovazione "REACT-EU" project (DM 1062/21).

Appendix A. Supporting information

Supplementary data associated with this article can be found in the online version at:doi:10.1016/j.cattod.2026.115978

Data Availability

Data will be made available on request.

References

[1] X. Zhang, B. Gao, A.E. Creamer, C. Cao, e.Y. Li, Adsorption of VOCs onto engineered carbon materials: a review, J. Hazard. Mater. 338 (2017) 102–123, https://doi.org/10.1016/j.jhazmat.2017.05.013.

[2] J. González-Martín, N.J.R. Kraakman, C. Pérez, R. Lebrero, e.R. Muñoz, A state–of–the-art review on indoor air pollution and strategies for indoor air pollution control, Chemosphere 262 (2021) 128376, https://doi.org/10.1016/j.chemosphere.2020.128376.

[3] B. Guieysse, C. Hort, V. Platel, R. Munoz, M. Ondarts, e S. Revah, Biological treatment of indoor air for VOC removal: potential and challenges, Biotechnol. Adv. 26 (fasc. 5) (2008) 398–410, https://doi.org/10.1016/j.biotechadv.2008.03.005.

[4] C.H. Halios, C. Landeg-Cox, S.D. Lowther, A. Middleton, T. Marczylo, e. S. Dimitroulopoulou, Chemicals in European residences – part I: a review of emissions, concentrations and health effects of volatile organic compounds (VOCs)», *Sci. Total. Environ.* 839 (2022) 156201 https://doi.org/10.1016/j.scitotenv.2022.156201.

[5] A. Krishnamurthy, B. Adebayo, T. Gelles, A. Rownaghi, e.F. Rezaei, Abatement of gaseous volatile organic compounds: a process perspective, Catal. Today 350 (2020) 100–119, https://doi.org/10.1016/j.cattod.2019.05.069.

[6] *WHO Guidelines for Indoor Air Quality: Selected Pollutants*. in WHO Guidelines Approved by the Guidelines Review Committee. Geneva: World Health Organization, 2010. Consultato: 28 ottobre 2025. [Online]. Disponibile su: http://www.ncbi.nlm.nih.gov/books/NBK138705/.

[7] M.S. Kamal, S.A. Razzak, e M. M Hossain, Catalytic oxidation of volatile organic compounds (VOCs) – a review, Atmos. Environ. 140 (2016) 117–134, https://doi.org/10.1016/j.atmosenv.2016.05.031.

[8] G. Pampararo, et al., Spray-made porous CuO-CeO2 microspheres rival precious metal catalysts for the low-temperature oxidation of air pollutants, J. Environ. Chem. Eng. 13 (fasc. 3) (2025) 116753, https://doi.org/10.1016/j.jece.2025.116753.

[9] N. Grifasi, et al., Copper-manganese oxide catalysts for low-temperature oxidation of indoor pollutants, Appl. Catal. B Environ. Energy 385 (2026) 126292, https://doi.org/10.1016/j.apcatb.2025.126292.

[10] X. Chen, W. Ma, e G Yang, Microenvironment regulation in zeolite-based catalysts for selective oxidation of aromatic VOCs, Catalysts 15 (fasc. 6) (2025) 581, https://doi.org/10.3390/catal15060581.

[11] N. Grifasi, et al., «Mesostructured manganese oxides for efficient catalytic oxidation of CO, ethylene, and propylene at mild temperatures: insight into the role of crystalline phases and physico-chemical properties», Appl. Catal. B Environ. Energy 362 (2025) 124696 https://doi.org/10.1016/j.apcatb.2024.124696.

[12] C. He, J. Cheng, X. Zhang, M. Douthwaite, S. Pattisson, e Z. Hao, Recent advances in the catalytic oxidation of volatile organic compounds: a review based on pollutant sorts and sources, Chem. Rev. 119 (fasc. 7) (2019) 4471–4568, https://doi.org/10.1021/acs.chemrev.8b00408.

[13] C. Chen, et al., Importance of platinum particle size for complete oxidation of toluene over Pt/ZSM-5 catalysts, Chem. Commun. 51 (fasc. 27) (2015) 5936–5938, https://doi.org/10.1039/C4CC09383F.

[14] T.N. Rostovshchikova, et al., ZSM-5 and BEA zeolites modified with Pd nanoparticles by laser electrodispersion. The structure and catalytic activity in CO and CH4 oxidation, Russ. Chem. Bull. 71 (fasc. 6) (2022) 1179–1193, https://doi.org/10.1007/s11172-022-3519-x.

[15] W. Zhang, P. Wang, C. Yang, e.C. Li, A comparative study of n-butane isomerization over H-Beta and H-ZSM-5 zeolites at low temperatures: effects of acid properties and pore structures, Catal. Lett. 149 (fasc. 4) (2019) 1017–1025, https://doi.org/10.1007/s10562-019-02683-0.

[16] R. El Khawaja, et al., VOCs catalytic removal over hierarchical porous zeolite NaY supporting Pt or Pd nanoparticles, Catal. Today 405–406 (2022) 212–220, https://doi.org/10.1016/j.cattod.2022.05.022.

[17] H. Yang, et al., Fluorine-enhanced Pt/ZSM-5 catalysts for low-temperature oxidation of ethylene, Catal. Sci. Technol. 8 (fasc. 7) (2018) 1988–1996, https://doi.org/10.1039/C8CY00130H.

[18] R. Ojeda-López, I.J. Pérez-Hermosillo, J.Marcos Esparza-Schulz, A. Cervantes-Uribe, e.A. Domínguez-Ortiz, SBA-15 materials: calcination temperature influence on textural properties and total silanol ratio, Adsorption 21 (fasc. 8) (2015) 659–669, https://doi.org/10.1007/s10450-015-9716-2.

[19] Y.T. Lai, et al., Pt/SBA-15 as a highly efficient catalyst for catalytic toluene oxidation, ACS Catal. 4 (fasc. 11) (2014) 3824–3836, https://doi.org/10.1021/cs500733j.

[20] J.M. Rosenholm, T. Czuryszkiewicz, F. Kleitz, J.B. Rosenholm, e M Lindén, On the nature of the Brønsted acidic groups on native and functionalized mesoporous siliceous SBA-15 as studied by benzylamine adsorption from solution, Langmuir 23 (fasc. 8) (2007) 4315–4323, https://doi.org/10.1021/la062450w.

[21] M. Luo, et al., «A paper-based plasma-assisted cataluminescence sensor for ethylene detection», Sens. Actuators B Chem. 240 (2017) 132–141, https://doi.org/10.1016/j.snb.2016.08.156.

[22] S.S. Satter, J. Hirayama, K. Nakajima, e.A Fukuoka, Low temperature oxidation of trace ethylene over Pt nanoparticles supported on hydrophobic mesoporous silica, *Chem. Lett.* 47 (fasc. 8) (2018) 1000–1002, https://doi.org/10.1246/cl.180364.

[23] A. Dorsey e United States, Toxicological profile for toluene, in: Toxicological profile for toluene (update), Agency for Toxic Substances and Disease Registry, Atlanta, Ga., 2000. https://catalog.hathitrust.org/Record/103205619 ([Online]. Disponibile su).

[24] J. Kim, et al., Catalytic ozonation of toluene using Mn–M bimetallic HZSM-5 (M: Fe, Cu, Ru, Ag) catalysts at room temperature, J. Hazard. Mater. 397 (2020) 122577, https://doi.org/10.1016/j.jhazmat.2020.122577.

[25] D. Murindababisha, et al., Current progress on catalytic oxidation of toluene: a review, Environ. Sci. Pollut. Res. 28 (fasc. 44) (2021) 62030–62060, https://doi.org/10.1007/s11356-021-16492-9.

[26] S. Jin, L. Zhong, X. Zhang, X. Li, B. Li, e.X. Fang, Indoor volatile organic compounds: concentration characteristics and health risk analysis on a university campus, Int. J. Environ. Res. Public. Health 20 (fasc. 10) (2023) 5829, https://doi.org/10.3390/ijerph20105829.

[27] Q. He, et al., Enhancing catalytic pyrolysis of polypropylene using mesopore-modified HZSM-5 catalysts: insights and strategies for improved performance, Front. Chem. Eng. 6 (2024) 1439400, https://doi.org/10.3389/fceng.2024.1439400.

[28] R. Peng, et al., Size effect of Pt nanoparticles on the catalytic oxidation of toluene over Pt/CeO2 catalysts, Appl. Catal. B Environ. 220 (2018) 462–470, https://doi.org/10.1016/j.apcatb.2017.07.048.

[29] H. Song, et al., Hydrothermal growth of mesoporous SBA-15 silica in the presence of PVP-stabilized Pt nanoparticles: synthesis, characterization, and catalytic properties, J. Am. Chem. Soc. 128 (fasc. 9) (2006) 3027–3037, https://doi.org/10.1021/ja057383r.

[30] Y. Wang, J. Ren, K. Deng, L. Gui, e.Y. Tang, Preparation of tractable platinum, rhodium, and ruthenium nanoclusters with small particle size in organic media, Chem. Mater. 12 (fasc. 6) (2000) 1622–1627, https://doi.org/10.1021/cm0000853.

[31] N. An, et al., Size effects of platinum colloid particles on the structure and CO oxidation properties of supported Pt/Fe $_2$ O $_3$ catalysts, J. Phys. Chem. C 117 (fasc. 41) (2013) 21254–21262, https://doi.org/10.1021/jp404266p.

[32] R.H. Crabtree, Aspects of methane chemistry, Chem. Rev. 95 (fasc. 4) (1995) 987–1007, https://doi.org/10.1021/cr00036a005.

[33] N. Felvey, et al., Interconversion of atomically dispersed platinum cations and platinum clusters in zeolite ZSM-5 and formation of platinum gem-dicarbonyls, J. Am. Chem. Soc. 144 (fasc. 30) (2022) 13874–13887, https://doi.org/10.1021/jacs.2c05386.

[34] A. Simperler, R.G. Bell, M.D. Foster, A.E. Gray, D.W. Lewis, e.M.W. Anderson, Probing the acid strength of Brønsted acidic zeolites with acetonitrile: an atomistic and quantum chemical study, J. Phys. Chem. B 108 (fasc. 22) (2004) 7152–7161, https://doi.org/10.1021/jp035673t.

[35] C. Otero Areán, et al., The combined use of acetonitrile and adamantane–carbonitrile as IR spectroscopic probes to discriminate between external and internal surfaces of medium pore zeolites, Microporous Mesoporous Mater. 34 (fasc. 1) (2000) 55–60, https://doi.org/10.1016/S1387-1811(99)00155-9.

[36] Y. Namgung, Y. Li, S. Kim, H.Y. Park, S. Saqlain, e.Y.D. Kim, A simple heat-treatment strategy to prepare hydrophobic zeolite ZSM-5 for efficient adsorption of toluene under humid conditions, Chem. Eng. J. 507 (2025) 160580, https://doi.org/10.1016/j.cej.2025.160580.

[37] D. Zhai, et al., A first-principles evaluation of the stability, accessibility, and strength of Brønsted acid sites in zeolites, J. Catal. 352 (2017) 627–637, https://doi.org/10.1016/j.jcat.2017.06.035.

[38] C. Chen, et al., Superior performance in catalytic combustion of toluene over KZSM-5 zeolite supported platinum catalyst, Catal. Lett. 144 (fasc. 11) (2014) 1851–1859, https://doi.org/10.1007/s10562-014-1295-4.

[39] S. Chytil, W.R. Glomm, e.E.A. Blekkan, Characterization of Pt/SBA-15 prepared by the deposition–precipitation method, Catal. Today 147 (fasc. 3–4) (2009) 217–223, https://doi.org/10.1016/j.cattod.2008.09.003.

[40] M.M.J. Treacy, J.B. Higgins, Collection of Simulated XRD Powder Patterns for Zeolites, 5th ed., Elsevier, Amsterdam, 2007.

[41] Y. Cheng, L.-J. Wang, J.-S. Li, Y.-C. Yang, e.X.-Y. Sun, Preparation and characterization of nanosized ZSM-5 zeolites in the absence of organic template, Mater. Lett. 59 (fasc. 27) (2005) 3427–3430, https://doi.org/10.1016/j.matlet.2005.06.008.

[42] Q. Zou, M. Liu, M. Fan, Y. Ding, Y. Chen, e.S. Shen, Effect of Na+ on catalytic performance of CoCe/ZSM-5 catalysts for oxidation of toluene, J. Rare Earths 39 (fasc. 4) (2021) 409–418, https://doi.org/10.1016/j.jre.2020.07.017.

[43] M.F.A. Aboud, Z.A. ALOthman, e.A.A. Bagabas, Storage and separation of methane and carbon dioxide using platinum- decorated activated carbons treated with ammonia, Mater. Res. Express 8 (fasc. 2) (2021) 025503, https://doi.org/10.1088/2053-1591/abe2e0.

[44] A. Sápi, et al., Synergetic of Pt nanoparticles and H-ZSM-5 zeolites for efficient CO2 activation: role of interfacial sites in high activity, Front. Mater. 6 (2019) 127, https://doi.org/10.3389/fmats.2019.00127.

[45] H. Zhao, e.H. Han, Synthesis and characterization of functionalized SBA-15 silica through template removal, J. Solid. State Chem. 282 (2020) 121074, https://doi.org/10.1016/j.jssc.2019.121074.

[46] M. Rachini, et al., Activity and selectivity of Bimetallic catalysts based on SBA-15 for nitrate reduction in water, Mater. Sci. Appl. 14 (fasc. 02) (2023) 78–93, https://doi.org/10.4236/msa.2023.142006.

[47] J. Lu, E. Bartholomeeusen, B.F. Sels, e.D. Schryvers, Internal architecture of coffin-shaped ZSM-5 zeolite crystals with hourglass contrast unravelled by focused ion beam-assisted transmission electron microscopy, J. Microsc. 265 (fasc. 1) (2017) 27–33, https://doi.org/10.1111/jmi.12459.

[48] A.A. Ahmed, e.Z.H. Yamani, Synthesis and characterization of SnO2-modified ZSM-5 zeolite for hydrogen gas sensing, Mater. Chem. Phys. 259 (2021) 124181, https://doi.org/10.1016/j.matchemphys.2020.124181.

[49] Y.-Q. Deng, W.-F. Zhou, H.-M. Lv, Y.-Y. Zhang, C.-T. Au, e.S.-F. Yin, Synthesis of HZSM-5@silicalite-1 core–shell composite and its catalytic application in the generation of p-xylene by methylation of toluene with methyl bromide, RSC Adv. 4 (fasc. 70) (2014) 37296–37301, https://doi.org/10.1039/C4RA04126G.

[50] J. Zhang, et al., Highly dispersed Pt nanoparticles supported on carbon nanotubes produced by atomic layer deposition for hydrogen generation from hydrolysis of ammonia borane, Catal. Sci. Technol. 7 (fasc. 2) (2017) 322–329, https://doi.org/10.1039/C6CY01960A.

[51] R. Peng, et al., Shape effect of Pt/CeO 2 catalysts on the catalytic oxidation of toluene, Chem. Eng. J. 306 (2016) 1234–1246, https://doi.org/10.1016/j.cej.2016.08.056.

[52] S. Chytil, W.R. Glomm, I. Kvande, T. Zhao, J.C. Walmsley, e.E.A. Blekkan, Platinum incorporated into the SBA-15 mesostructure via deposition-precipitation method: Pt nanoparticle size estimation and catalytic testing», *Top. Catal.* 45 (fasc. 1–4) (2007) 93–99, https://doi.org/10.1007/s11244-007-0246-3.

[53] D.E. Romero, M. Rigutto, e.E.J.M. Hensen, Influence of the size, order and topology of mesopores in bifunctional Pd-containing acidic SBA-15 and M41S catalysts for n-hexadecane hydrocracking, Fuel Process. Technol. 232 (2022) 107259, https://doi.org/10.1016/j.fuproc.2022.107259.

[54] K. Leung, I.M.B. Nielsen, e.L.J. Criscenti, Elucidating the Bimodal Acid-base Behavior of the Water-silica Interface from First Principles, J. Am. Chem. Soc. 131 (fasc. 51) (2009) 18358–18365, https://doi.org/10.1021/ja906190t.

[55] C. Karakaya, e.O. Deutschmann, A simple method for CO chemisorption studies under continuous flow: adsorption and desorption behavior of Pt/Al2O3 catalysts, Appl. Catal. Gen. 445–446 (2012) 221–230, https://doi.org/10.1016/j.apcata.2012.08.022.

[56] H.-H. Liu, Y. Wang, A.-P. Jia, S.-Y. Wang, M.-F. Luo, e.J.-Q. Lu, Oxygen vacancy promoted CO oxidation over Pt/CeO 2 catalysts: a reaction at Pt–CeO 2 interface, Appl. Surf. Sci. 314 (2014) 725–734, https://doi.org/10.1016/j.apsusc.2014.06.196.

[57] M.-R. Kim, e.S. Kim, Enhanced catalytic oxidation of toluene over hierarchical Pt/Y zeolite, *Catalysts* 12 (fasc. 6) (2022) 622, https://doi.org/10.3390/catal12060622.

[58] I.O. Ali, et al., Synthesis, structural configuration and DFT molecular orbital studies of [Mn-2[benzo[b]oxazole] acetonitrile] complexes encapsulated in ZSM-5: direct synthesis of phenol by benzene hydroxylation, Microporous Mesoporous Mater. 262 (2018) 35–48, https://doi.org/10.1016/j.micromeso.2017.10.042.

[59] Y. Wang, et al., Investigation of catalytic ozonation of recalcitrant organic chemicals in aqueous solution over various ZSM-5 zeolites, Catalysts 8 (fasc. 4) (2018) 128, https://doi.org/10.3390/catal8040128.

[60] I.R. Shaikh, et al., H-ZSM-5 zeolite synthesis by sourcing silica from the wheat husk ash: characterization and application as a versatile heterogeneous catalyst in organic transformations including some multicomponent reactions, *J. Catal.* 2015 (fasc. 1) (2015) 805714, https://doi.org/10.1155/2015/805714.

[61] L. Shirazi, E. Jamshidi, e M.R. Ghasemi, The effect of Si/Al ratio of ZSM-5 zeolite on its morphology, acidity and crystal size, Cryst. Res. Technol. 43 (fasc. 12) (2008) 1300–1306, https://doi.org/10.1002/crat.200800149.

[62] S. Bordiga, E. Escalona Platero, C. Otero Areán, C. Lamberti, A. Zecchina, Low temperature CO adsorption on Na-ZSM-5 zeolites: An FTIR investigation, J. Catal. 137 (fasc. 1) (1992) 179–185, https://doi.org/10.1016/0021-9517(92)90147-A.

[63] R. Buzzoni, S. Bordiga, G. Ricchiardi, C. Lamberti, A. Zecchina, e.G. Bellussi, Interaction of pyridine with acidic (H-ZSM5, H-β, H-MORD zeolites) and superacidic (H-Nafion Membrane) systems: an IR investigation, *Langmuir* 12 (fasc. 4) (1996) 930–940, https://doi.org/10.1021/la950571i.

[64] L.M. Kustov, V.B. Kazanskii, Stanislav. Beran, Ludmila. Kubelkova, e.Pavel. Jiru, Adsorption of carbon monoxide on ZSM-5 zeolites: infrared spectroscopic study and quantum-chemical calculations, J. Phys. Chem. 91 (fasc. 20) (1987) 5247–5251, https://doi.org/10.1021/j100304a023.

[65] E. Giglio, et al., Tailoring the acidity of ZSM-5 via surface passivation: Catalytic assessment on dimethyl ether to olefins (DTO) process, Fuel 362 (2024) 130559, https://doi.org/10.1016/j.fuel.2023.130559.

[66] M. Giuliano, et al., Characterization of the evolution of noble metal particles in a commercial three-way catalyst: correlation between real and simulated ageing, Catalysts 11 (fasc. 2) (2021) 247, https://doi.org/10.3390/catal11020247.

[67] F. Wakabayashi, J.N. Kondo, K. Domen, e.C. Hirose, Direct comparison of N2 and CO as IR-spectroscopic probes of acid sites in H-ZSM-5 zeolite, J. Phys. Chem. 99 (fasc. 26) (1995) 10573–10580, https://doi.org/10.1021/j100026a021.

[68] K. Hadjiivanov, H. Knözinger, e.M. Mihaylov, FTIR study of CO adsorption on Ni−ZSM-5, J. Phys. Chem. B 106 (fasc. 10) (2002) 2618–2624, https://doi.org/10.1021/jp0132782.

[69] A. Zecchina, S. Bordiga, C. Lamberti, G. Spoto, L. Carnelli, e.C. Otero Arean, Low-temperature fourier transform infrared study of the interaction of CO with cations in alkali-metal exchanged ZSM-5 zeolites, J. Phys. Chem. 98 (fasc. 38) (1994) 9577–9582, https://doi.org/10.1021/j100089a035.

[70] S.R. Batool, V.L. Sushkevich, e.J.A. Van Bokhoven, Correlating Lewis acid activity to extra-framework aluminum species in zeolite Y introduced by Ion-exchange, J. Catal. 408 (2022) 24–35, https://doi.org/10.1016/j.jcat.2022.02.010.

[71] K. Chakarova, e.K. Hadjiivanov, Problems in the IR measuring the acidity of zeolite bridging hydroxyls by low-temperature CO adsorption, Chem. Commun. 47 (fasc. 6) (2011) 1878–1880, https://doi.org/10.1039/C0CC04484A.

[72] J. Datka, B. Gil, M. Kawałek, e.B. Staudte, Low temperature IR studies of CO sorbed in ZSM-5 zeolites, J. Mol. Struct. 511–512 (1999) 133–139, https://doi.org/10.1016/S0022-2860(99)00151-9.

[73] H.V. Brand, A. Redondo, e.P.J. Hay, Theoretical studies of CO adsorption on H-ZSM-5 and hydrothermally treated H-ZSM-5, J. Mol. Catal. Chem. 121 (fasc. 1) (1997) 45–62, https://doi.org/10.1016/S1381-1169(96)00456-6.

[74] K. Chakarova, M. Mihaylov, e.K. Hadjiivanov, FTIR spectroscopic study of CO adsorption on Pt–H–ZSM-5, Microporous Mesoporous Mater. 81 (fasc. 1–3) (2005) 305–312, https://doi.org/10.1016/j.micromeso.2005.01.033.

[75] J. Gajardo, et al., Revealing the effects of high Al loading incorporation in the SBA-15 silica mesoporous material, J. Porous Mater. 30 (fasc. 5) (2023) 1687–1707, https://doi.org/10.1007/s10934-023-01453-z.

[76] C. Otero Areán, M. Peñarroya Mentruit, M. Rodríguez Delgado, G. Turnes Palomino, O.V. Manoilova, A.A. Tsyganenko, E. Garrone, Variable temperature FTIR spectroscopy of carbon monoxide adsorbed on protonic and rubidium-exchanged ZSM-5 zeolites, in: Studies in Surface Science and Catalysis, Elsevier, 2002, pp. 207–214, https://doi.org/10.1016/S0167-2991(02)80030-1.

[77] T. Armaroli, M. Trombetta, A. Gutièrrez Alejandre, J. Ramirez Solis, e.G. Busca, FTIR study of the interaction of some branched aliphatic molecules with the external and internal sites of H-ZSM5 zeolite, Phys. Chem. Chem. Phys. 2 (fasc. 14) (2000) 3341–3348, https://doi.org/10.1039/b001807o.

[78] A.V. Yakimov, V.L. Sushkevich, J.A. Van Bokhoven, e.C. Copéret, Probing acid sites in MOR zeolite using low-temperature^{13} C solid-state NMR spectroscopy of adsorbed carbon monoxide, J. Phys. Chem. C 126 (fasc. 7) (2022) 3681–3687, https://doi.org/10.1021/acs.jpcc.1c10026.

[79] G. Yablonsky, R. Fushimi, e.G.B. Marin, Kinetic measurements in heterogeneous catalysis, in: Kirk-Othmer, A c. di (Eds.), Kirk-Othmer Encyclopedia of Chemical Technology, 1, Wiley, 2021, pp. 1–44, https://doi.org/10.1002/0471238961.1109140513010704.a01.pub3.

[80] X. Zhu, et al., CeO2-supported pt catalysts derived from MOFs by two pyrolysis strategies to improve the oxygen activation ability, Nanomaterials 10 (fasc. 5) (2020) 983, https://doi.org/10.3390/nano10050983.

[81] M. Chen, et al., Promoting low-temperature toluene oxidation via Pt–O–Fe interfacial sites in a Pt/CuO–Fe_3 O_4 catalyst, Environ. Sci. Technol. 59 (fasc. 22) (2025) 11365–11376, https://doi.org/10.1021/acs.est.5c02048.

[82] M. Zhou, et al., Enhanced hydrophobic microporous Pt/silica with high adsorption and catalytic oxidation for trace toluene removal, J. Environ. Chem. Eng. 11 (fasc. 5) (2023) 110821, https://doi.org/10.1016/j.jece.2023.110821.

[83] J. Cui, et al., Efficient catalytic oxidation of toluene over a hierarchical porous Pt/ZSM-5/MCM-41 catalyst, J. Environ. Chem. Eng. 14 (fasc. 3) (2026) 122278, https://doi.org/10.1016/j.jece.2026.122278.

[84] R.M. Silverstein, F.X. Webster, D.J. Kiemle, e D.L. Bryce. Spectrometric Identification of Organic Compounds, 8th ed., John Wiley & Sons, 2014. ISBN 978-0-470-61637-6.
[85] Z. Jiang, D. Chen, X. Wang, Y. Jia, W. Deng, e.L. Guo, Highly active and stable plate-like ZSM-5 supported MnOx catalysts for toluene oxidation: effect of preparation methods, Appl. Surf. Sci. 640 (2023) 158252, https://doi.org/10.1016/j.apsusc.2023.158252.
[86] M.J. Hossain, M.M. Rahman, e.Md.Jafar Sharif, Preference for low-coordination sites by adsorbed CO on small platinum nanoparticles, Nanoscale Adv. 2 (fasc. 3) (2020) 1245–1252, https://doi.org/10.1039/C9NA00499H.
[87] A. Lu, et al., Surface partial-charge-tuned enhancement of catalytic activity of platinum nanocatalysts for toluene oxidation, ACS Catal. 9 (fasc. 8) (2019) 7431–7442, https://doi.org/10.1021/acscatal.9b01776.
[88] X. Peng, L. Liu, B. Shen, Y. Bian, e.L. Su, Insight into the catalytic oxidation of toluene over M/ZSM-5 (M=Cu, Mn, Fe, Ce, Ti) catalysts, J. Fuel Chem. Technol. 51 (fasc. 6) (2023) 841–851, https://doi.org/10.1016/S1872-5813(22)60069-0.
[89] B.C. Smith, The C=O Bond, Part IV: Acid Anhydrides, Spectroscopy 33 (fasc. 3) (2018) 16–20.